Nitrate Reduction to Ammonia Catalyzed by GaN / Si Photoelectrodes with Metal Clusters

Wan Jae Dong,[1,2,‡] Jan Paul Menzel,[3,‡] Kejian Li,[1] Zhengwei Ye,[1] Zhuoran Long,[3] Ishtiaque Ahmed Navid,[1] Ke R. Yang,[3] Yixin Xiao,[1] Victor S. Batista,[3,*] and Zetian Mi[1,*]

[1] Department of Electrical Engineering and Computer Science, University of Michigan, 1301 Beal Avenue, Ann Arbor, Michigan 48109, USA

[2] Department of Integrative Energy Engineering, Graduate School of Energy and Environment (KU-KIST Green School), College of Engineering, Korea University, Seoul 02841, Republic of Korea.

[3] Department of Chemistry, Yale University, New Haven, Connecticut 06520-8107, USA

[‡]W. J. Dong and J. P. Menzel contributed equally to this work.

[*]E-mail: ztmi@umich.edu, victor.batista@yale.edu

EXPERIMENTAL SECTION

Calculation of faradaic efficiency and production rate

The faradaic efficiency (FE) of NO_3^- reduction reaction was calculated as follows:

$$FE_{NH3} = \frac{8 \times F \times C_{NH3} \times V}{17 \times Q}$$

$$FE_{NO2-} = \frac{2 \times F \times C_{NO2-} \times V}{46 \times Q}$$

$$FE_{N2H4} = \frac{14 \times F \times C_{N2H4} \times V}{32 \times Q}$$

The produdction rate of each product of NH_3, NO_2^-, and N_2H_4 was calculated using the following equation:

$$Y_{NH3} = \frac{C_{NH3} \times V}{17 \times t \times A}$$

$$Y_{NO2-} = \frac{C_{NO2-} \times V}{46 \times t \times A}$$

$$Y_{N2H4} = \frac{C_{N2H4} \times V}{32 \times t \times A}$$

where F is the Faraday constant (96,485 C/mol), V is the volume of the cathoid electrolyte (8 ml), Q is the total charge flowed, t is the reaction time, and A is the geometric surface area of photoelectrodes. C_{NH3}, C_{NO2-}, and C_{N2H4} are the measured NH_3, NO_2^-, and N_2H_4 concentrations, respectively.

Computational details

DFT calculations were performed using the VASP.5 (Vienna Ab initio Simulation Package) program.[1, 2, 3] Core electrons were treated using the PAW (Projector Augmented Wave) method.[4, 5] The PBE functional[6] was used in combination with D3 dispersion corrections with BJ-damping to describe dispersion interactions.[7, 8] A cutoff energy of 450 eV was employed. Optimizations were performed until the convergence citeria of $1x10^{-6}$ eV/unit cell of energy and 0.02eV/Å maximum force were reached. A Methfessel-Paxton smearing method with a sigma value of 0.1 eV was added to maintain finite temperature electronic populations.[9] For Co_3O_4, DFT+U with a U_{eff} value of 3.0 eV as suggested by Selcuk and Selloni was used for correct electronic structure and surface reactivity.[10] The Co and Cu slabs were generated from bulk optimizations using an fcc cell with 4 atoms for Cu, with 15x15x15 kpoint mesh, and a 3*3*1 hcp Co cell with 18 atoms, using a 11x11x21 Monkhorst-Pack type k-grid.[11] The lowest

energy for Co was determined when using a spin polarization of 28 more alpha then beta electrons (1.56 unpaired electrons per Co atom). The Co_3O_4 slab was constructed from an optimized bulk Co_3O_4 using the spinel structure including 24 cobalt and 56 oxygen atoms with a 11x11x11 kpoint mesh and a larger cutoff of 600 eV. The resulting geometry and spin structure is given in Figure S34a, which includes Co(III) atoms without unpaired electrons and Co(II) atoms with three unpaired electrons ferromagnetically coupled within a plane to the other Co(II) atoms, while parallel planes are antiferromagnetically coupled to one another with a total of 12 unpaired α spins and 12 unpaired β spins.

The $Ni(OH)_2$ bulk was built using the starting structure from reference [12], using a U_{eff} value of 5.5 eV, as suggested by Kim *et al.* [13] and a 15x15x15 K-point grid with 600 eV cutoff energy. NiOOH bulk was constructed from this structure, using a 13x21x3 K-point grid and removing every second hydrogen atom before reoptimizing. The slabs for Co and Cu were constructed from the bulk structures, using the (111) surfaces, 4 layers in z, each containing of 3x3 atoms. A K-point mesh of 3x3x1 was used, with periodic boundary conditions in all dimensions, but a large vacuum layer in c direction to prohibit interaction between the slabs. The box dimensions were a=7.557 Å, b=7.556 Å and c= 35.000 Å for the Cu slab and a=7.557 Å, b=7.556 Å and c= 35.000 Å for the Co slab, whose most stable spin state was 57 unpaired electrons (1.58 per Co atom). The lowest two layers were frozen to maintain bulk geometry and properties, while the upper two layers were allowed to relax. For Cobalt, several different spin states were calculated for each intermediate, using the lowest energy one for the Gibbs free energy differences. For Cobalt oxide, the 100-S surface was constructed as in reference.[10] The lower layers were subsequently frozen. The resulting box dimensions were a=8.079 Å, b=8.079 Å and c= 40.000 Å. A cutoff energy of 450 eV and a k-grid of 1x1x1 was employed. Figure S38b shows the geometry and spin structure of the finalized surface.

To construct the $Ni(OH)_2$ (001) surface, two layers of each 4 Ni, 8 O and 8 H atoms were used from the bulk geometry, resulting in a total of 40 atoms. Using a cutoff energy of 450 eV, a U_{eff}=5.5 eV, 3x3x1 K-point mesh, the upper layer was allowed to relax while the lower was frozen in bulk geometry. The box dimensions were a=5.408 Å, b= 6.245 Å and c=35.000Å to guarantee a large vacuum layer to prevent self-interaction. A figure including the spin density that shows the ferromagnetically coupled Ni atoms within one layer with antiferromagnetic coupling between the sheets, is given in Figure S43. The NiOOH (001) surface was constructed from the bulk, using 2 sheets consisting of 4 Ni, 8 O and 4 H respectively, with a total of 32 atoms. The lowest layer was frozen, while the upper was allowed to relax. A cutoff energy of

450 eV was used with a K-point grid of 3x3x1. An effective U_{eff} of 5.5 eV was applied. The box dimensions are a=5.028 Å, b= 5.800 Å and c=35.000Å

Gibbs free energy was determined through the following scheme: geometry optimizations were performed in vacuum, followed by a finite difference approach vibrational analysis with a step of 0.4 Bohr only including the adsorbate atoms. Using the harmonic approximation at 298 K and 1 atm, Gibbs free energy corrections were determined with the obtained results utilizing the vaspkit1.3 package.[14] These free energy corrections were added to energies obtained with a geometry optimization in implicit water solvent (dielectric constant of 80.0) performed with the VASPsol extension.[15] Energies obtained in solution, free energy corrections and Gibbs free energies for all intermediates are given in Tables S2-S6. Visualization of the intermediates was done with VESTA.[16]

Photoelectrochemical NO_3^- reduction on Co_3O_4

Formal chemical equations for the nitrate reduction on Co_3O_4 are given in the equations below:

$$* NO_3^- + * H^+ + Co_n^{II}Co_{2n}^{III}O_{4n} + H^+ + e^- \rightarrow * NO_3^- + [Co_{n+1}^{II}Co_{2n-1}^{III}O_{4n-1}]^+ + H_2O$$

$$* NO_3^- + [Co_{n+1}^{II}Co_{2n-1}^{III}O_{4n-1}]^+ \rightarrow * NO_2 + Co_n^{II}Co_{2n}^{III}O_{4n}$$

$$* NO_2 + H^+ + e^- \rightarrow * NO_2^- + * H^+$$

$$* NO_2^- + * H^+ + Co_n^{II}Co_{2n}^{III}O_{4n} + H^+ + e^- \rightarrow * NO_2^- + [Co_{n+1}^{II}Co_{2n-1}^{III}O_{4n-1}]^+ + H_2O$$

$$* NO_2^- + [Co_{n+1}^{II}Co_{2n-1}^{III}O_{4n-1}]^+ \rightarrow * NO + Co_n^{II}Co_{2n}^{III}O_{4n}$$

$$* NO + H^+ + e^- \rightarrow * NHO$$

$$* NHO + H^+ + e^- \rightarrow * NH_2O$$

$$* NH_2O + H^+ + e^- \rightarrow * NH_2OH$$

$$* NH_2OH + H^+ + e^- \rightarrow * NH_2 + H_2O$$

$$* NH_2 + H^+ + e^- + HNO_3 \rightarrow * NO_3^- + * H^+ + NH_3$$

$$HNO_3 + 8H^+ + 8e^- \rightarrow NH_3 + 3H_2O$$

In Figure S41, the relative Gibbs free energy of the steps in photoelectrochemical NO_3^- reduction on Co_3O_4 are given. The intermediates are also visualized using the optimized structure in implicit solvent. Energies, free energy correction terms and Gibbs free energies are

given in Table S4, including possible magnetization for intermediates with uneven number of electrons.

Photoelectrochemical NO_3^- reduction on Cu

In Figure S36, the relative Gibbs free energy of the steps in photoelectrochemical NO_3^- reduction on Cu are given, with both possible pathways of full reduction to ammonia and incomplete reduction to NO_2^-. The intermediates are also visualized using the optimized structure in implicit solvent. Energies, free energy correction terms and Gibbs free energies are given in Table S2.

Photoelectrochemical NO_3^- reduction on Co

In Figure S37, the relative Gibbs free energy of the steps in photoelectrochemical NO_3^- reduction on Co are given, with both possible pathways of full reduction to ammonia and incomplete reduction to NO_2^-. The intermediates are also visualized using the optimized structure in implicit solvent. Energies, free energy correction terms and Gibbs free energies are given in Table S3, including possible spin states.

Photoelectrochemical NO_3^- reduction on NiOOH and $Ni(OH)_2$

We found that NiOOH readily reduces to $Ni(OH)_2$ in contact with protons and already positive potentials as shown in Figure S42. Therefore, all following calculations were performed on $Ni(OH)_2$. $Ni(OH)_2$ readily forms defects with acids and is therefore reactive towards both nitric acid and nitrous acid. The formal chemical equations of NO_3^- reduction on $Ni(OH)_2$ are as follows:

$$HNO_3 + Ni(OH)_2 \rightarrow [NiOH]^+ + NO_3^- + H_2O \rightarrow Ni(OH)(O) * NO_2 + H_2O$$

$$Ni(OH)(O) * NO_2 + H^+ + e^- \rightarrow Ni(OH)_2 + NO_2$$

$$2NO_2 + H_2O \rightarrow HNO_3 + HNO_2$$

$$HNO_2 + Ni(OH)_2 \rightarrow [NiOH]^+ + NO_2^- + H_2O \rightarrow Ni(OH)(O) * NO + H_2O$$

$$Ni(OH)(O) * NO + H^+ + e^- \rightarrow Ni(OH)_2 + NO$$

$$Ni(OH)_2 + NO + H^+ + e^- \rightarrow Ni(OH)(O) * N + H_2O$$

$$Ni(OH)(O) * N + H^+ + e^- \rightarrow Ni(OH)(O) * NH$$

$$Ni(OH)(O) * NH + H^+ + e^- \rightarrow Ni(OH)(O) * NH_2$$

$$Ni(OH)(O) * NH_2 + H^+ + e^- \rightarrow Ni(OH)(O) + NH_3$$

$$Ni(OH)(O) + H^+ + e^- \rightarrow Ni(OH)_2$$

$$\boldsymbol{HNO_3 + 8H^+ + 8e^- \rightarrow 3H_2O + NH_3}$$

The relative Gibbs free energy of the steps involved are given in Figure S44, with the optimized DFT structures in implicit solvent. Energies, free energy correction terms and Gibbs free energies are given in Table S5.

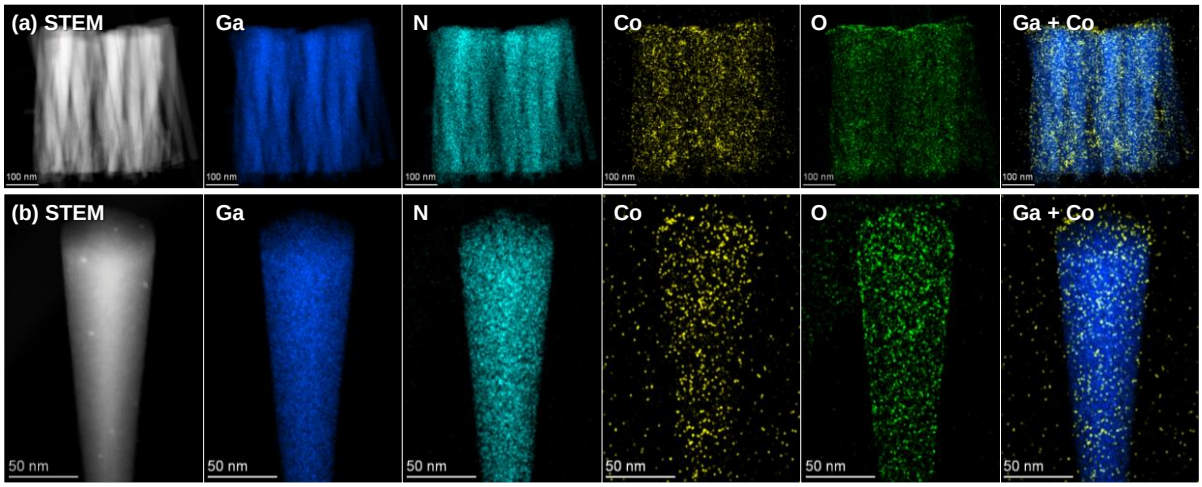

Figure S1. Structure and composition analysis of Co/GaN/Si. High-angle annular dark field scanning transmission electron microscopy (HAADF-STEM) images and energy dispersive spectroscopy (EDS) elemental maps of (a) Co-coated GaN NW bundles and (b) Co-coated single GaN NW.

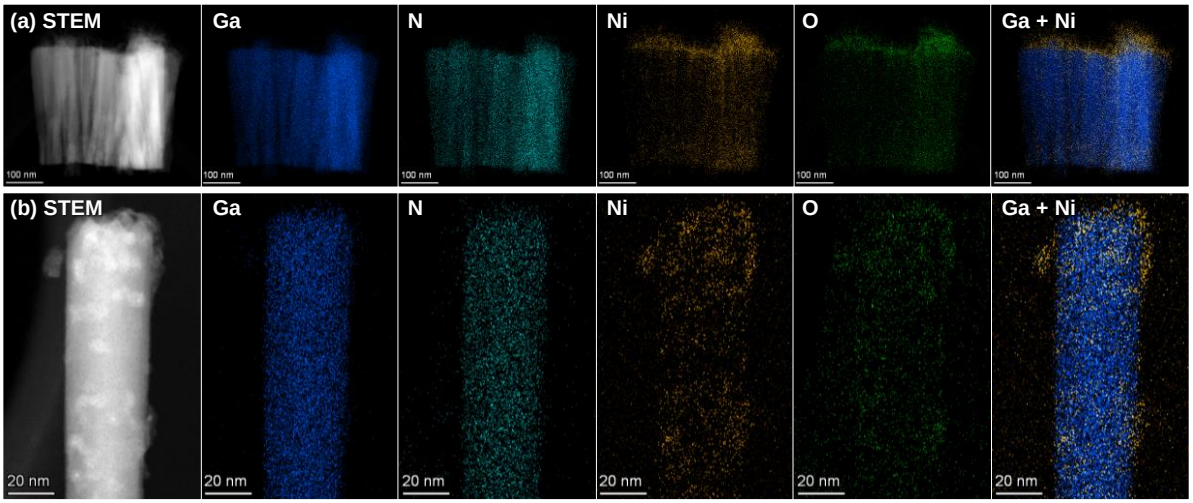

Figure S2. Structure and composition analysis of Ni/GaN/Si. High-angle annular dark field scanning transmission electron microscopy (HAADF-STEM) images and energy dispersive spectroscopy (EDS) elemental maps of (a) Ni-coated GaN NW bundles and (b) Ni-coated single GaN NW.

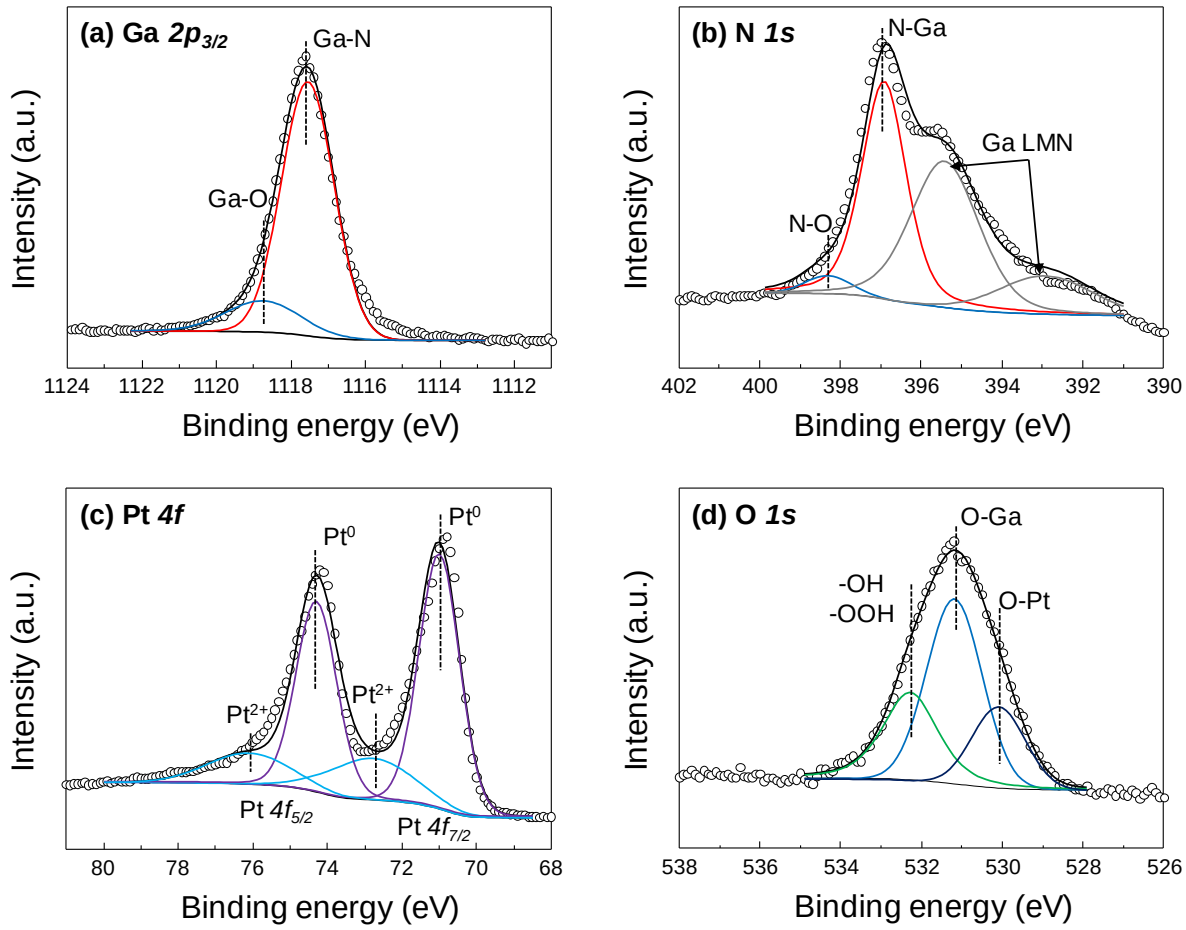

Figure S3. XPS analysis of Pt/GaN/Si. XPS spectra of (a) Ga *2p*$_{2/3}$, (b) N *1s*, (c) Pt *4f*, and (d) O *1s* for Pt/GaN/Si. The catalyst consists of metallic Pt and oxides.

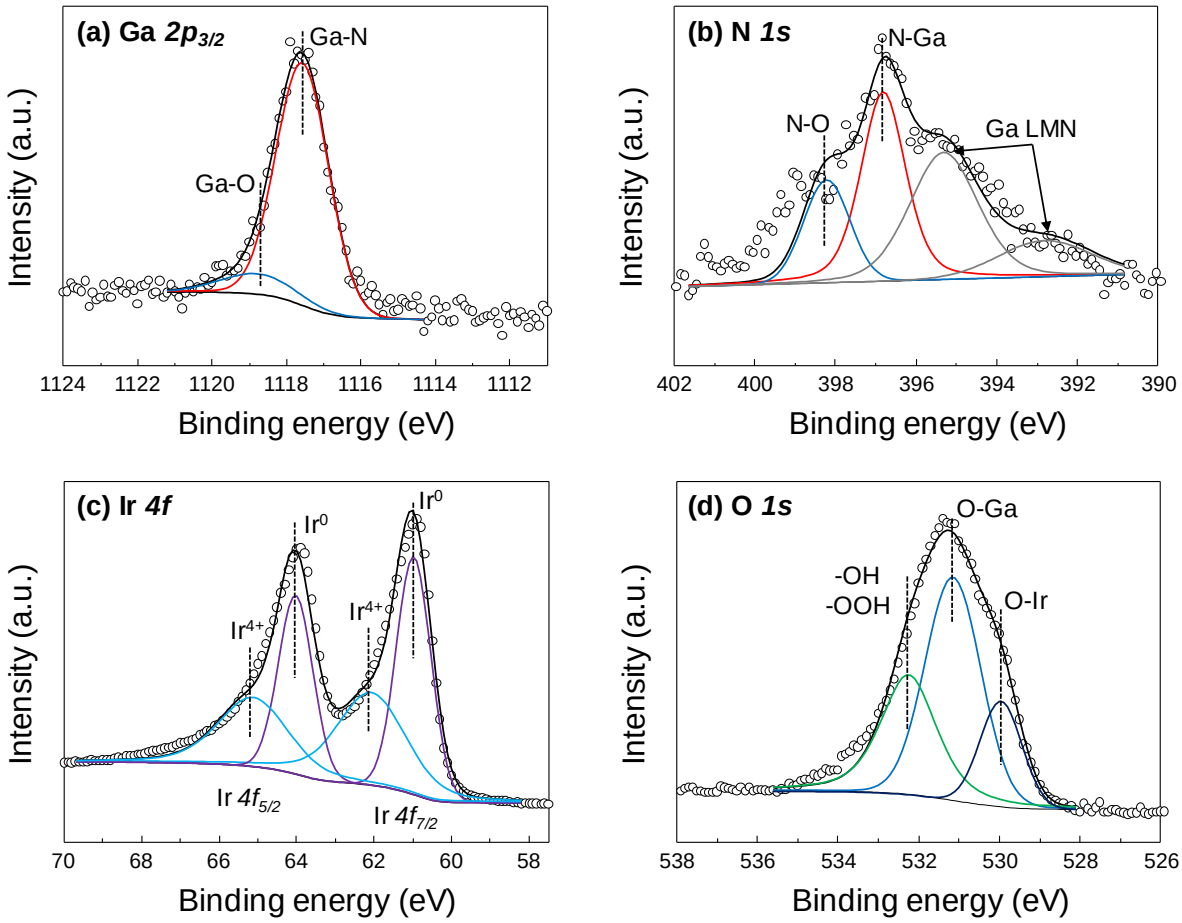

Figure S4. XPS analysis of Ir/GaN/Si. XPS spectra of (a) Ga $2p_{2/3}$, (b) N *1s*, (c) Ir *4f*, and (d) O *1s* for Ir/GaN/Si. The catalyst consists of metallic Ir and oxides.

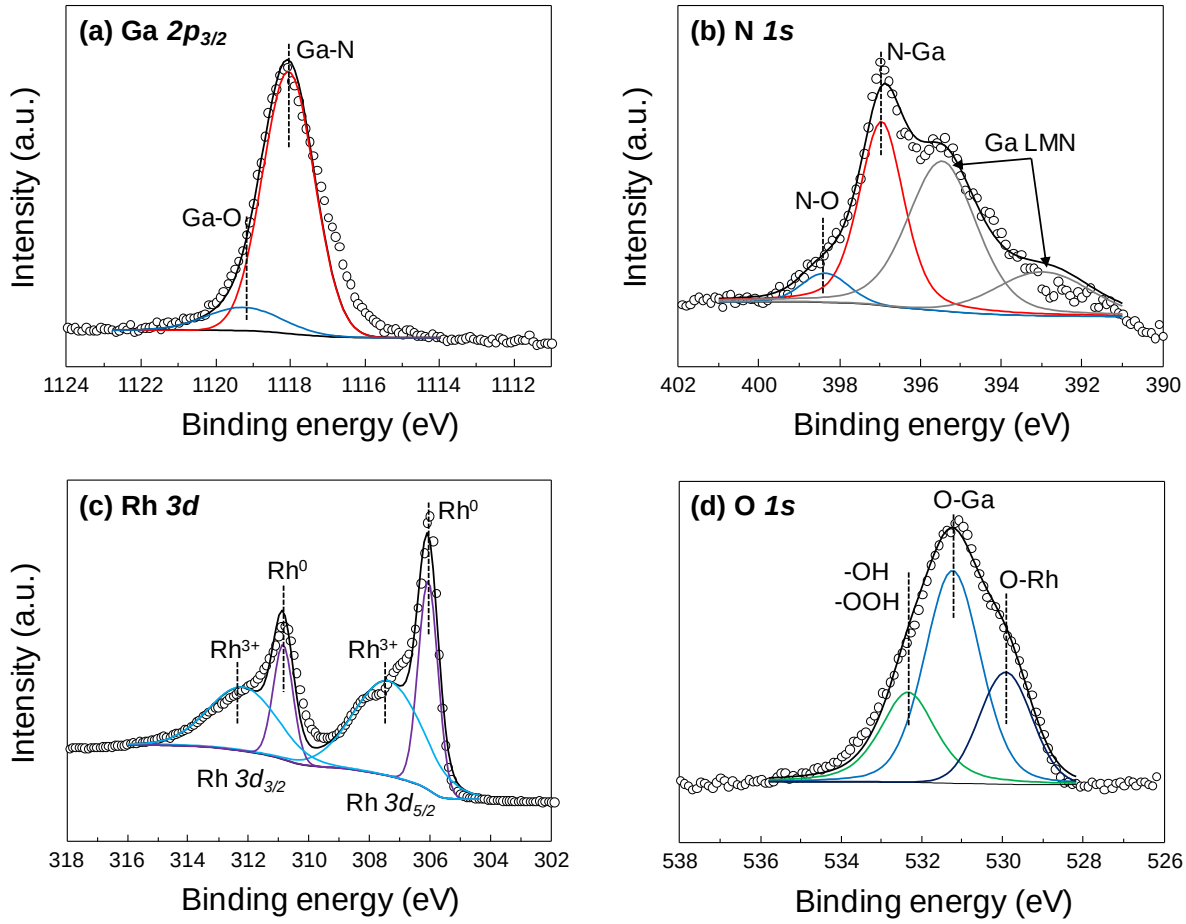

Figure S5. XPS analysis of Rh/GaN/Si. XPS spectra of (a) Ga *2p*$_{2/3}$, (b) N *1s*, (c) Rh *3d*, and (d) O *1s* for Rh/GaN/Si. The catalyst consists of metallic Rh and oxides.

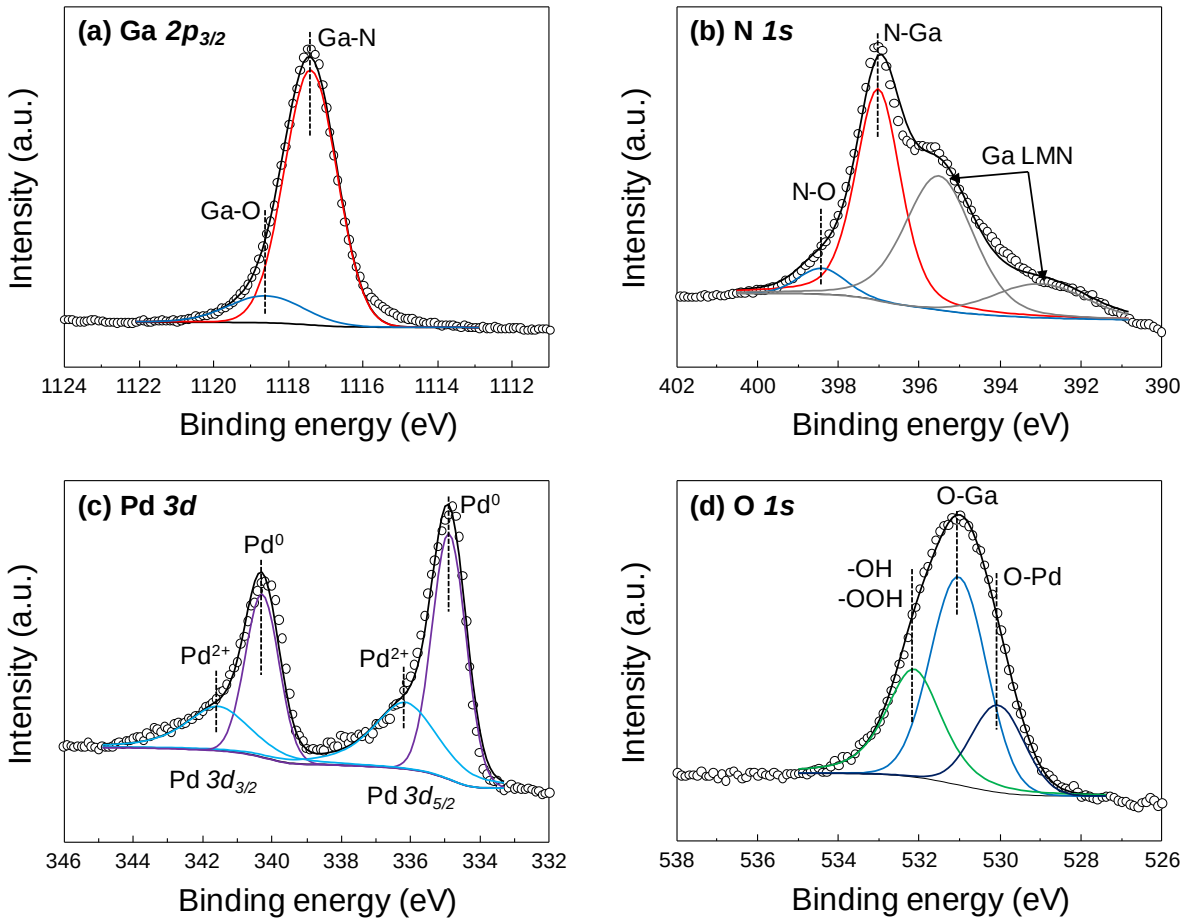

Figure S6. XPS analysis of Pd/GaN/Si. XPS spectra of (a) Ga *2p*$_{2/3}$, (b) N *1s*, (c) Pd *3d*, and (d) O *1s* for Pd/GaN/Si. The catalyst consists of metallic Pd and oxides.

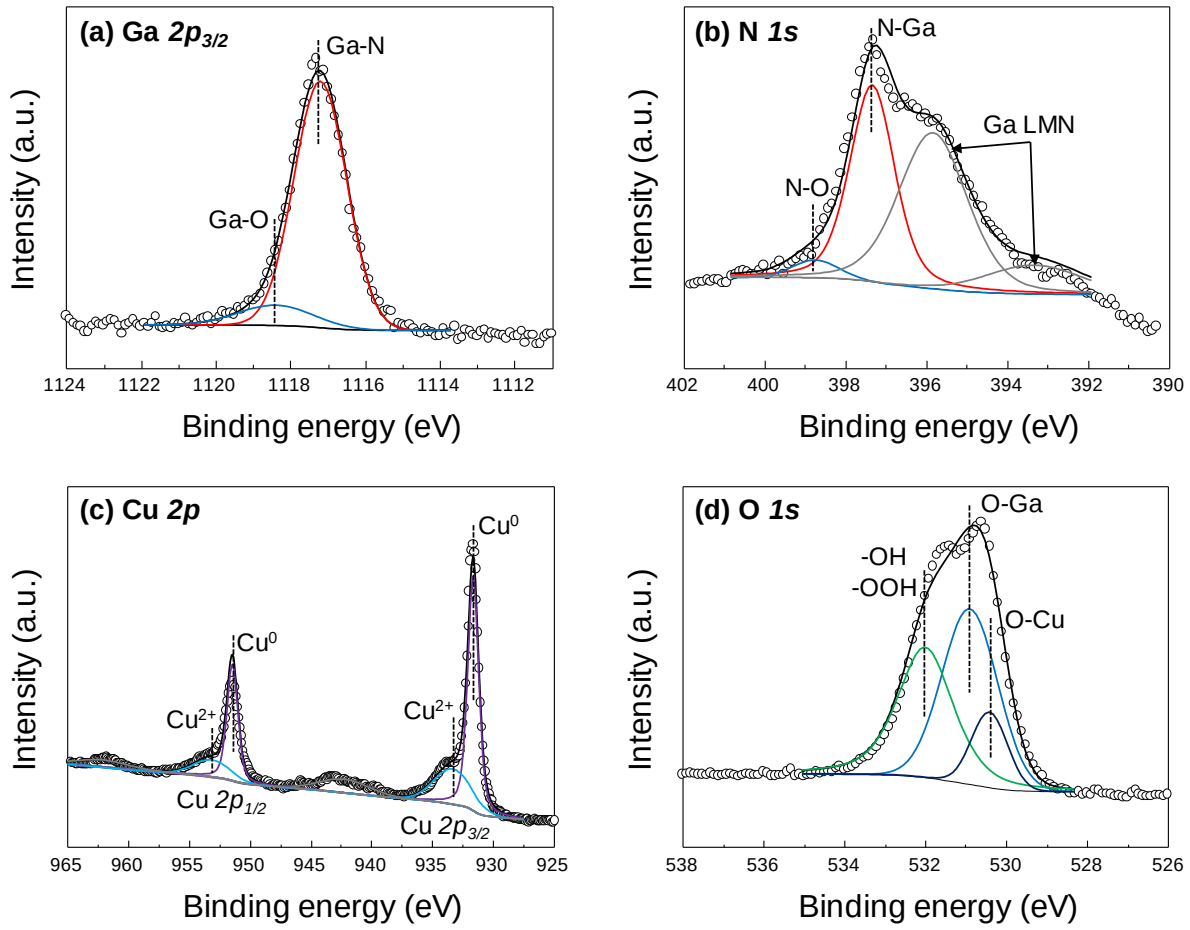

Figure S7. XPS analysis of Cu/GaN/Si. XPS spectra of (a) Ga $2p_{2/3}$, (b) N *1s*, (c) Cu *2p*, and (d) O *1s* for Cu/GaN/Si. The catalyst consists of metallic Cu and oxides.

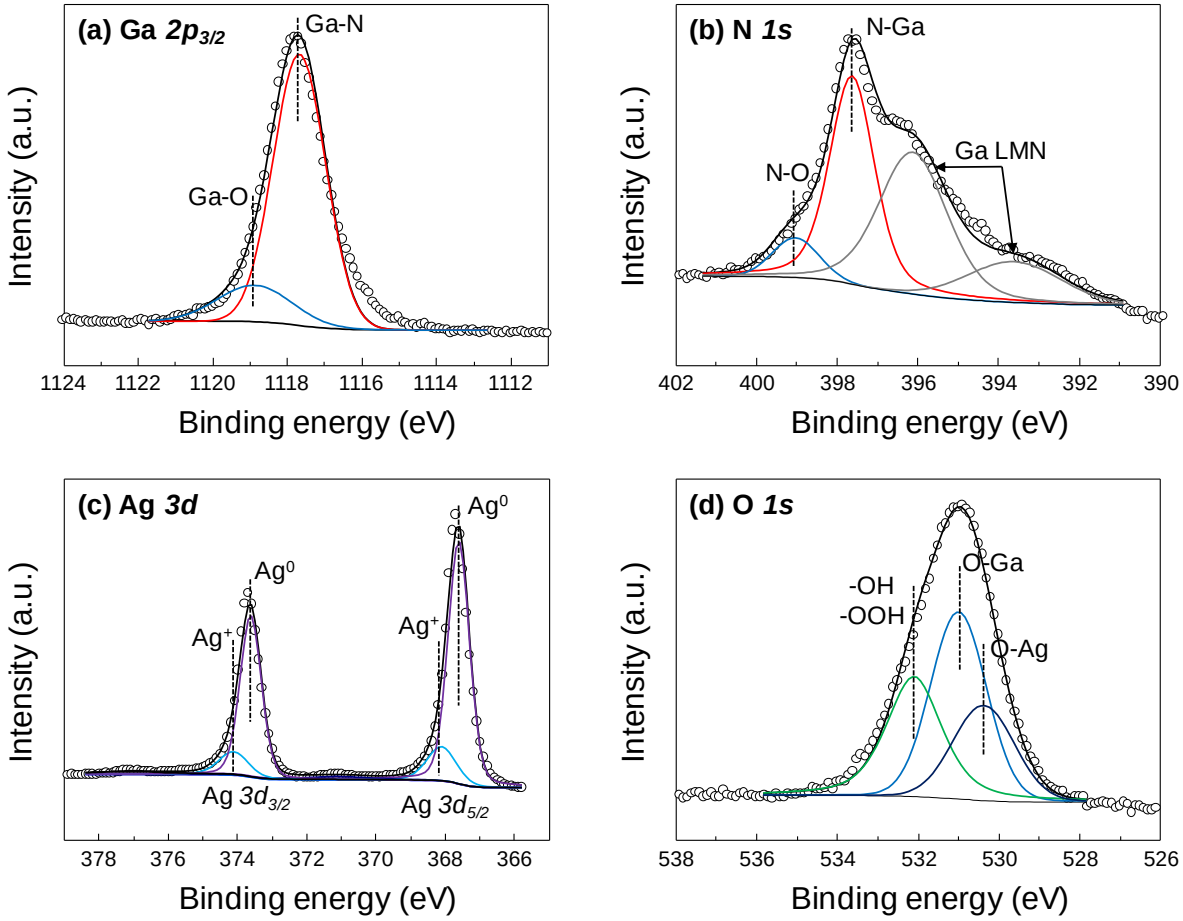

Figure S8. XPS analysis of Ag/GaN/Si. XPS spectra of (a) Ga *2p*$_{2/3}$, (b) N *1s*, (c) Ag *3d*, and (d) O *1s* for Ag/GaN/Si. The catalyst consists of metallic Ag and oxides.

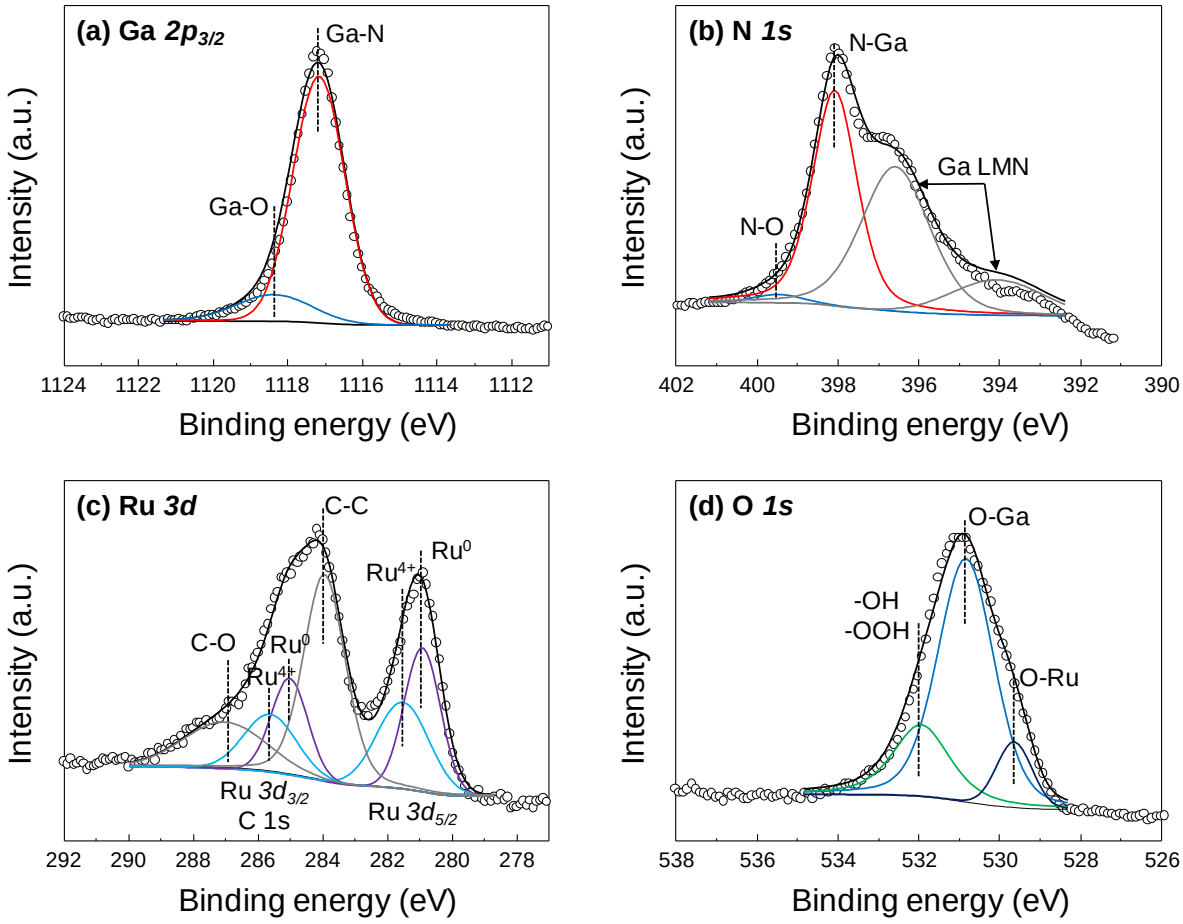

Figure S9. XPS analysis of Ru/GaN/Si. XPS spectra of (a) Ga *2p*$_{2/3}$, (b) N *1s*, (c) Ru *3d*, and (d) O *1s* for Ru/GaN/Si. The catalyst consists of metallic Ru and oxides.

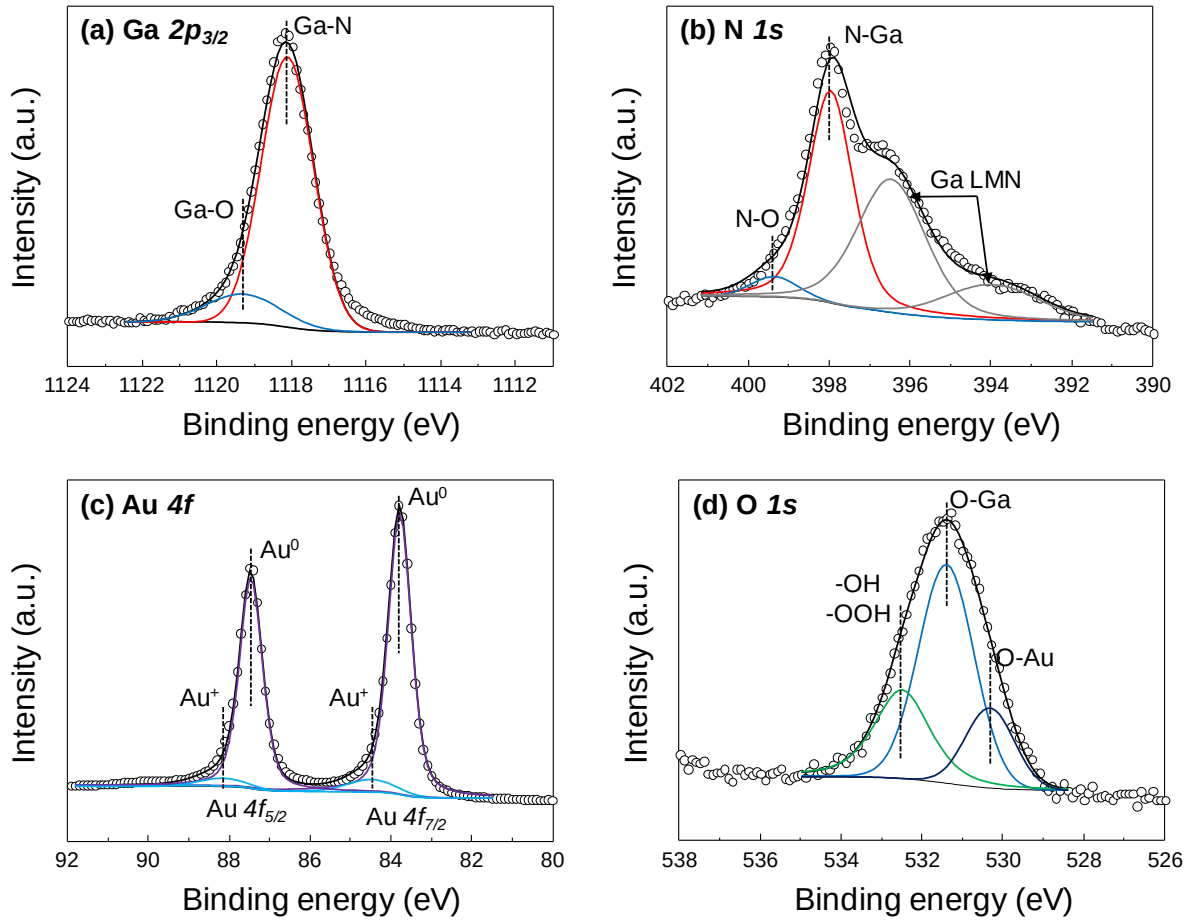

Figure S10. XPS analysis of Au/GaN/Si. XPS spectra of (a) Ga $2p_{2/3}$, (b) N *1s*, (c) Ag *4f*, and (d) O *1s* for Au/GaN/Si. The catalyst consists of metallic Au and oxides.

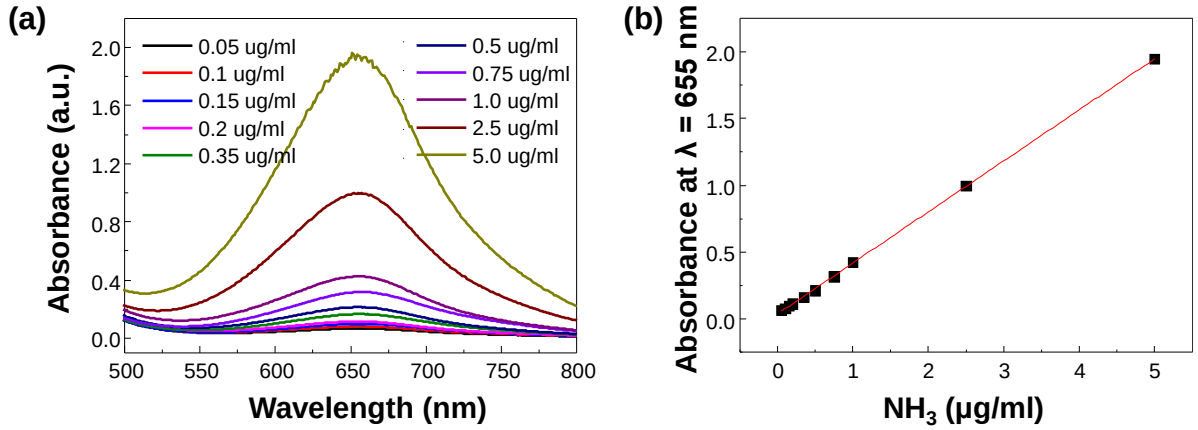

Figure S11. NH_3 calibration. (a) UV-visible absorbance spectra of indophenol assays with NH_3 ions and (b) calibration curve of NH_3.

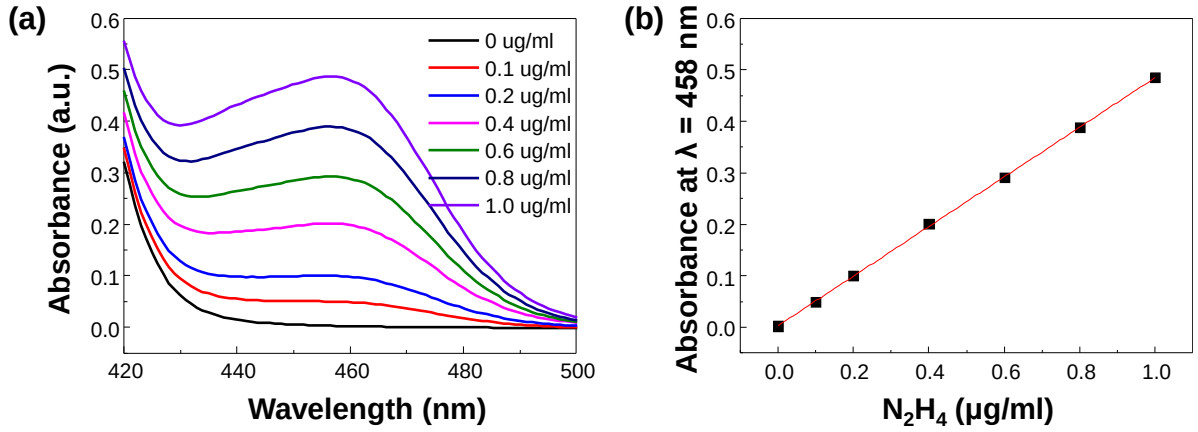

Figure S12. N_2H_4 calibration. (a) UV-visible absorbance spectra and (b) calibration curve of N_2H_4.

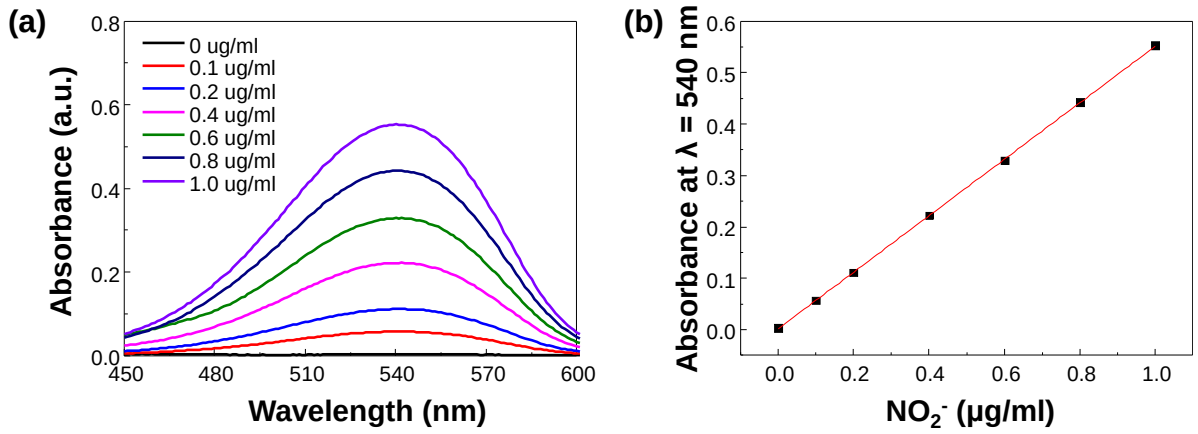

Figure S13. NO_2^- calibration. (a) UV-visible absorbance spectra and (b) calibration curve of NO_2^-.

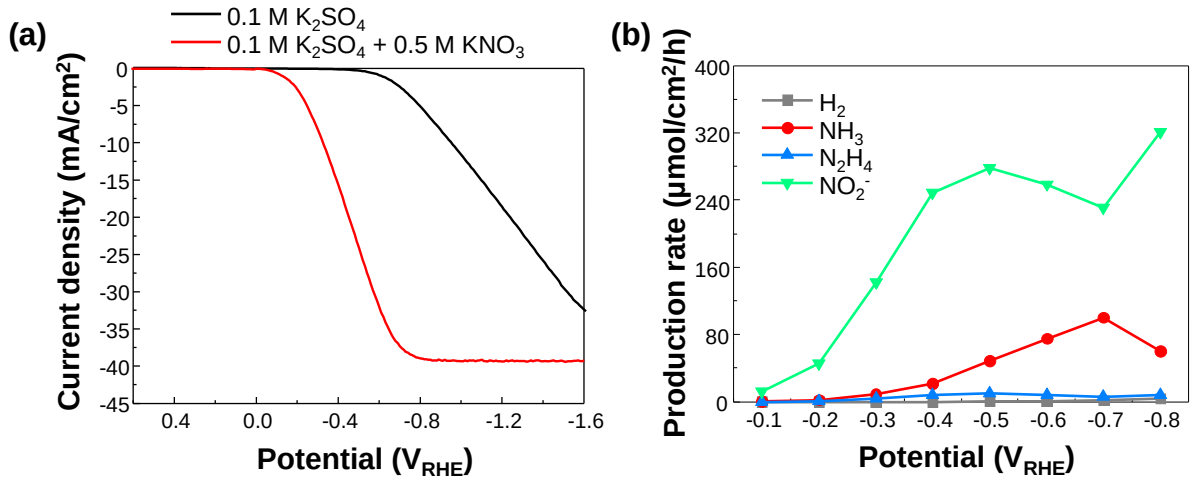

Figure S14. Photoelectrochemical measurement of GaN/Si. (a) LSV curves of GaN/Si measured in 0.1 M K_2SO_4 (black) and 0.1 M K_2SO_4 with 0.5 M KNO_3 (red) under AM 1.5G 1-sun light illumination. (b) Production rate of H_2, NH_3, N_2H_4, and NO_2^- at various potentials.

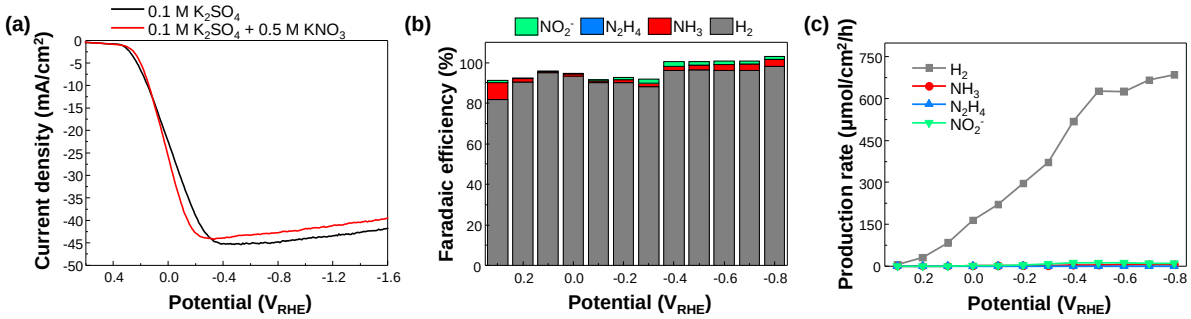

Figure S15. Photoelectrochemical measurement of Pt/GaN/Si. (a) LSV curves of Pt/GaN/Si measured in 0.1 M K_2SO_4 (black) and 0.1 M K_2SO_4 with 0.5 M KNO_3 (red) under AM 1.5G 1-sun light illumination. (b) Faradaic efficiency and (c) production rate of H_2, NH_3, N_2H_4, and NO_2^- at various potentials.

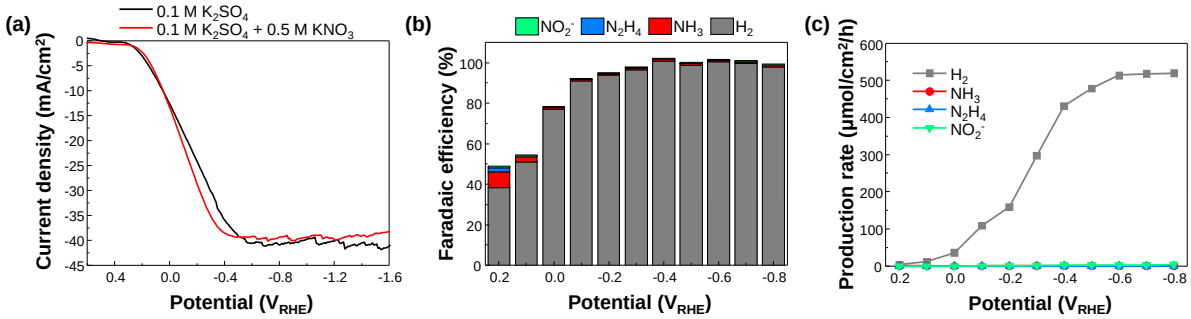

Figure S16. Photoelectrochemical measurement of Ir/GaN/Si. (a) LSV curves of Ir/GaN/Si measured in 0.1 M K_2SO_4 (black) and 0.1 M K_2SO_4 with 0.5 M KNO_3 (red) under AM 1.5G 1-sun light illumination. (b) Faradaic efficiency and (c) production rate of H_2, NH_3, N_2H_4, and NO_2^- at various potentials.

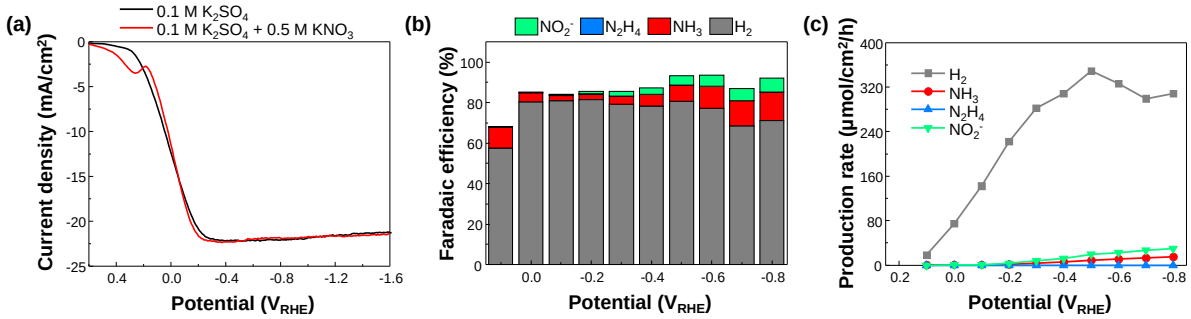

Figure S17. Photoelectrochemical measurement of Rh/GaN/Si. (a) LSV curves of Rh/GaN/Si measured in 0.1 M K_2SO_4 (black) and 0.1 M K_2SO_4 with 0.5 M KNO_3 (red) under AM 1.5G 1-sun light illumination. (b) Faradaic efficiency and (c) production rate of H_2, NH_3, N_2H_4, and NO_2^- at various potentials.

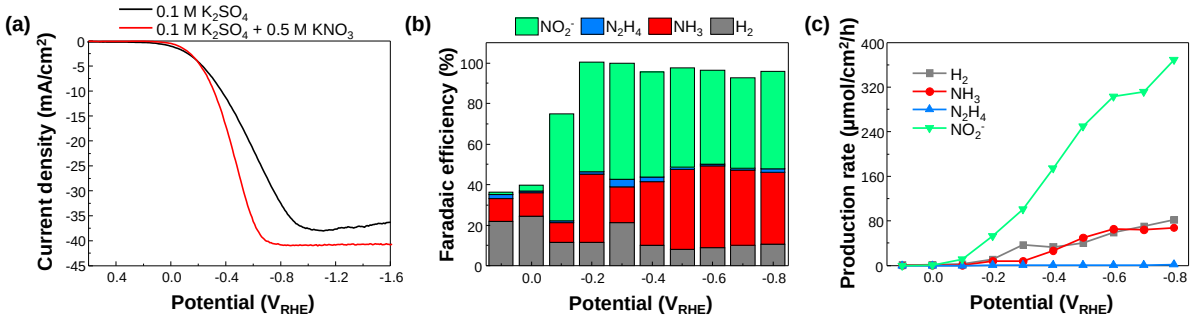

Figure S18. Photoelectrochemical measurement of Pd/GaN/Si. (a) LSV curves of Pd/GaN/Si measured in 0.1 M K_2SO_4 (black) and 0.1 M K_2SO_4 with 0.5 M KNO_3 (red) under AM 1.5G 1-sun light illumination. (b) Faradaic efficiency and (c) production rate of H_2, NH_3, N_2H_4, and NO_2^- at various potentials.

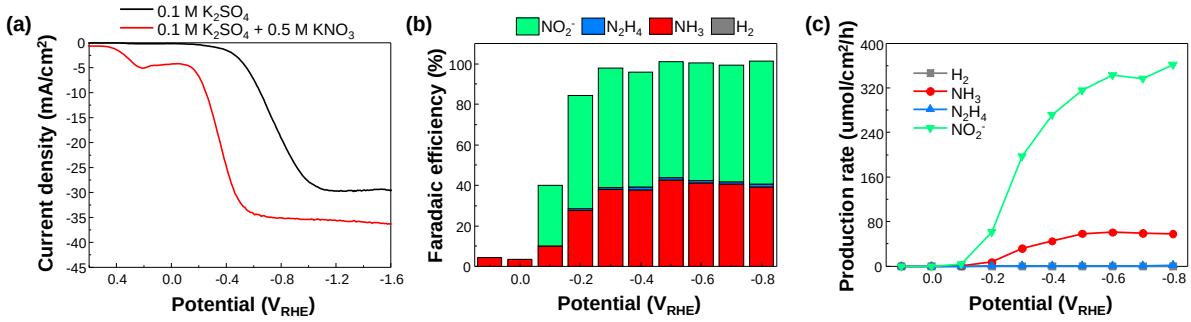

Figure S19. Photoelectrochemical measurement of Ag/GaN/Si. (a) LSV curves of Ag/GaN/Si measured in 0.1 M K_2SO_4 (black) and 0.1 M K_2SO_4 with 0.5 M KNO_3 (red) under AM 1.5G 1-sun light illumination. (b) Faradaic efficiency and (c) production rate of H_2, NH_3, N_2H_4, and NO_2^- at various potentials.

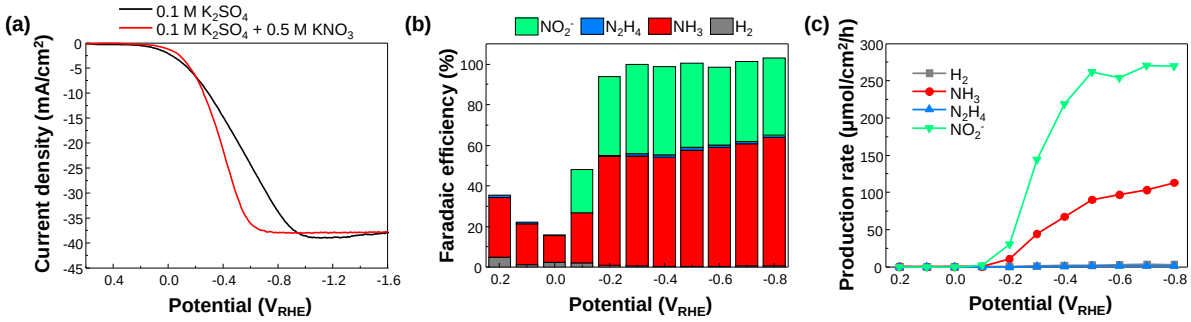

Figure S20. Photoelectrochemical measurement of Ru/GaN/Si. (a) LSV curves of Ru/GaN/Si measured in 0.1 M K_2SO_4 (black) and 0.1 M K_2SO_4 with 0.5 M KNO_3 (red) under AM 1.5G 1-sun light illumination. (b) Faradaic efficiency and (c) production rate of H_2, NH_3, N_2H_4, and NO_2^- at various potentials.

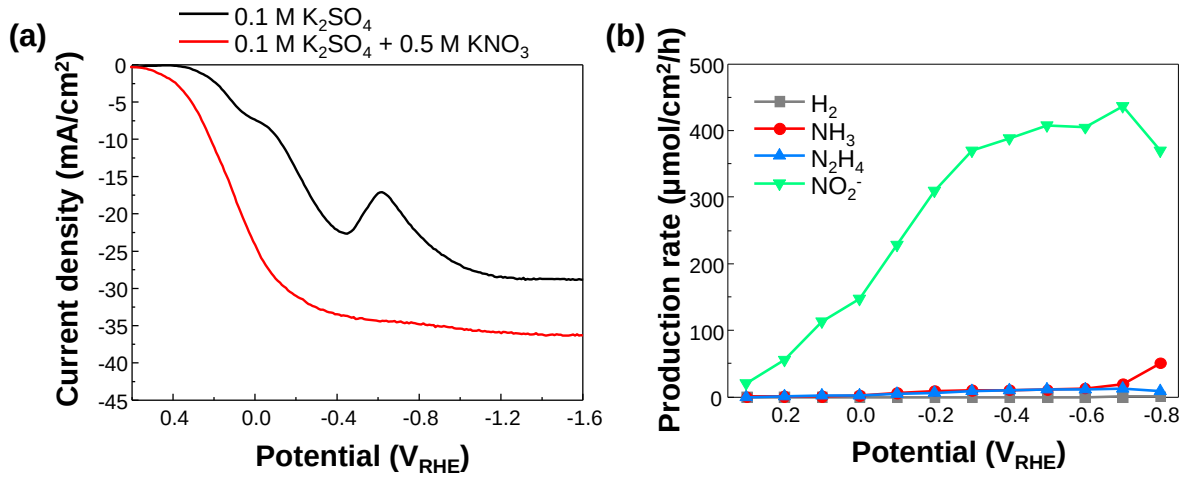

Figure S21. Photoelectrochemical measurement of Cu/GaN/Si. (a) LSV curves of Cu/GaN/Si measured in 0.1 M K_2SO_4 (black) and 0.1 M K_2SO_4 with 0.5 M KNO_3 (red) under AM 1.5G 1-sun light illumination. (b) Production rate of H_2, NH_3, N_2H_4, and NO_2^- at various potentials.

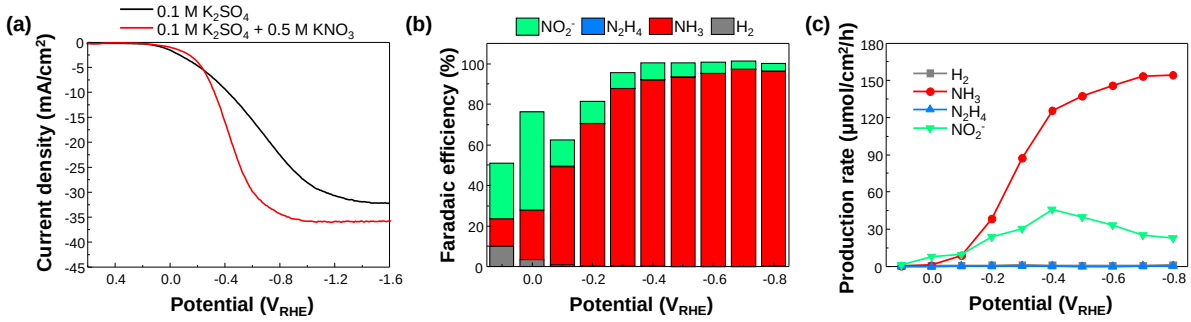

Figure S22. Photoelectrochemical measurement of Au/GaN/Si. (a) LSV curves of Au/GaN/Si measured in 0.1 M K_2SO_4 (black) and 0.1 M K_2SO_4 with 0.5 M KNO_3 (red) under AM 1.5G 1-sun light illumination. (b) Faradaic efficiency and (c) production rate of H_2, NH_3, N_2H_4, and NO_2^- at various potentials.

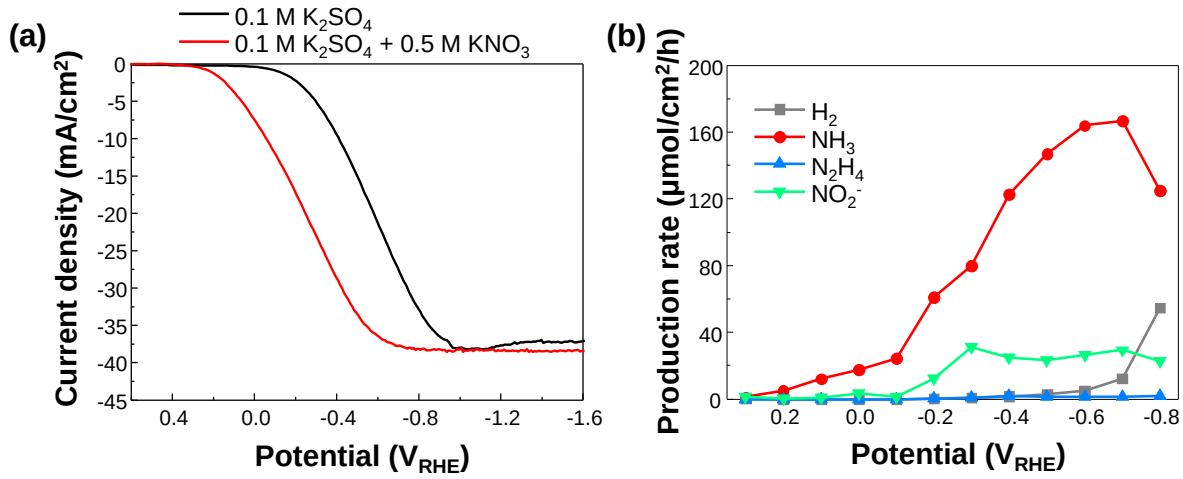

Figure S23. Photoelectrochemical measurement of Co/GaN/Si. (a) LSV curves of Co/GaN/Si measured in 0.1 M K_2SO_4 (black) and 0.1 M K_2SO_4 with 0.5 M KNO_3 (red) under AM 1.5G 1-sun light illumination. (b) Production rate of H_2, NH_3, N_2H_4, and NO_2^- at various potentials.

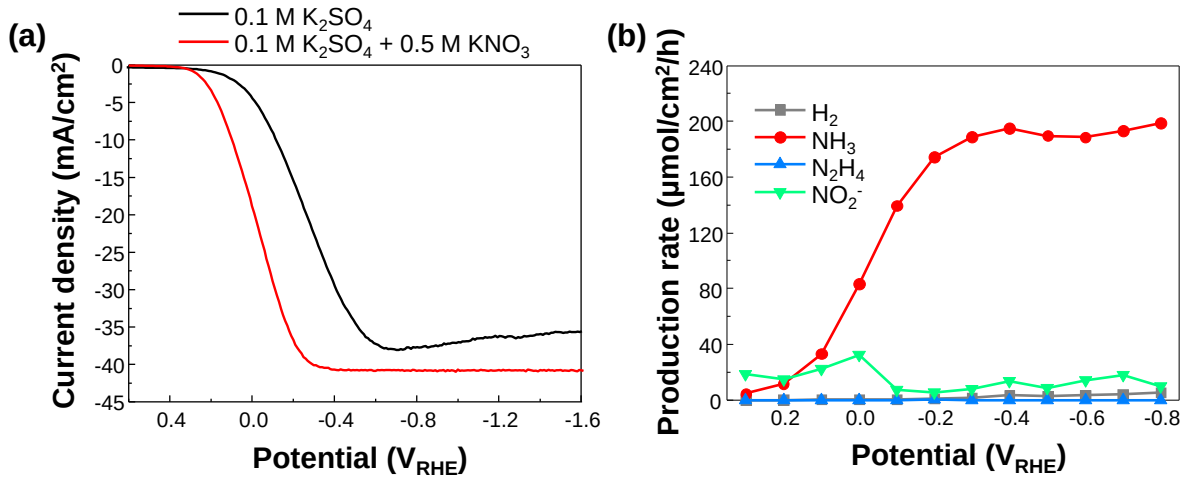

Figure S24. Photoelectrochemical measurement of Ni/GaN/Si. (a) LSV curves of Ni/GaN/Si measured in 0.1 M K_2SO_4 (black) and 0.1 M K_2SO_4 with 0.5 M KNO_3 (red) under AM 1.5G 1-sun light illumination. (b) Production rate of H_2, NH_3, N_2H_4, and NO_2^- at various potentials.

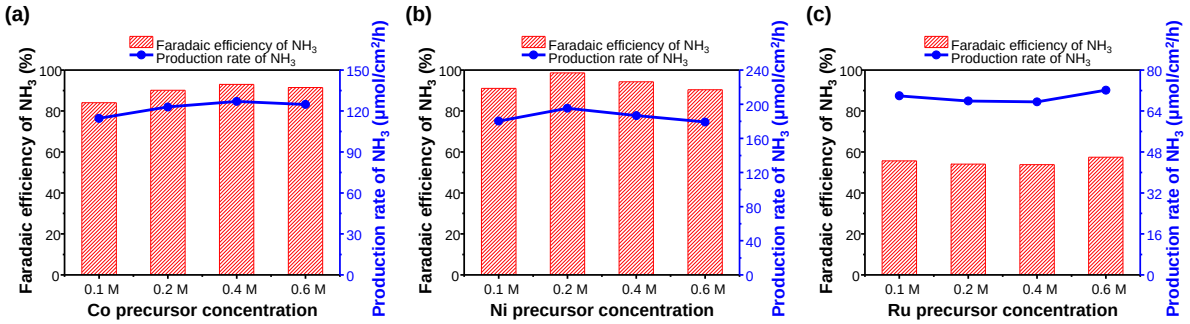

Figure S25. Optimization of precursor concentration for photodeposition. Faradaic efficiency and production rate of NH_3 for (a) Co/GaN/Si, (b) Ni/GaN/Si, and (c) Ru/GaN/Si photoelectrodes. Loading amount of metal catalysts was varied by changing the concentration of precursor solution for photodeposition process.

To investigate the effects of the loading amount of metal catalysts coated on GaN NWs on catalytic properties, we varied the precursor concentration used for Co, Ni, and Ru photodeposition and measured the faradaic efficiency and production rate of NO_3^- reduction to NH_3 at -0.4 V_{RHE} in 0.5 M KNO_3 solution (Figure S25). The photodeposition process was conducted in a 66 mL aqueous solution containing 20 vol% methanol, with the addition of 10 μl of metal precursor solutions. Specifically, Co, Ni, and Ru were deposited using solutions with concentrations of 0.1 – 0.6 M $CoCl_2$, 0.2 M $Ni(NO_3)_2$, and 0.4 M $RuCl_3$, respectively. For the Co/GaN/Si photoelectrode, FE_{NH3} was 85% at a concentration of 0.1 M, while at concentrations of 0.2, 0.4, and 0.6 M, FE_{NH3} reached levels of 90-93%, with corresponding production rates of NH_3 ranging from 123 to 127 μmol/cm^2/h (Figure S25a). Ni/GaN/Si exhibited FE_{NH3} exceeding 90% and production rates ranging from 180 to 195 μmol/cm^2/h across all concentration ranges (Figure S25b). In the case of Ru/GaN/Si, FE_{NH3} was approximately 55% and production rates were in the range of 67 to 72 μmol/cm^2/h (Figure S25c).

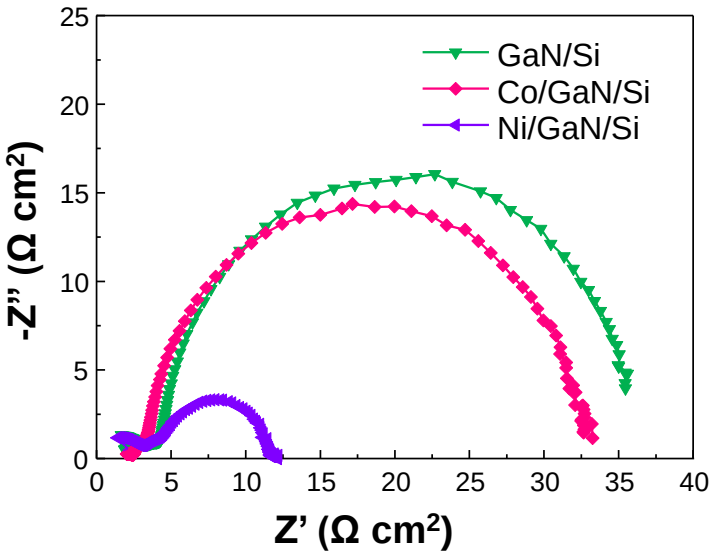

Figure S26. Impedance analysis. Nyquist plots of GaN/Si, Co/GaN/Si, and Ni/GaN/Si measured at -0.2 V_{RHE}.

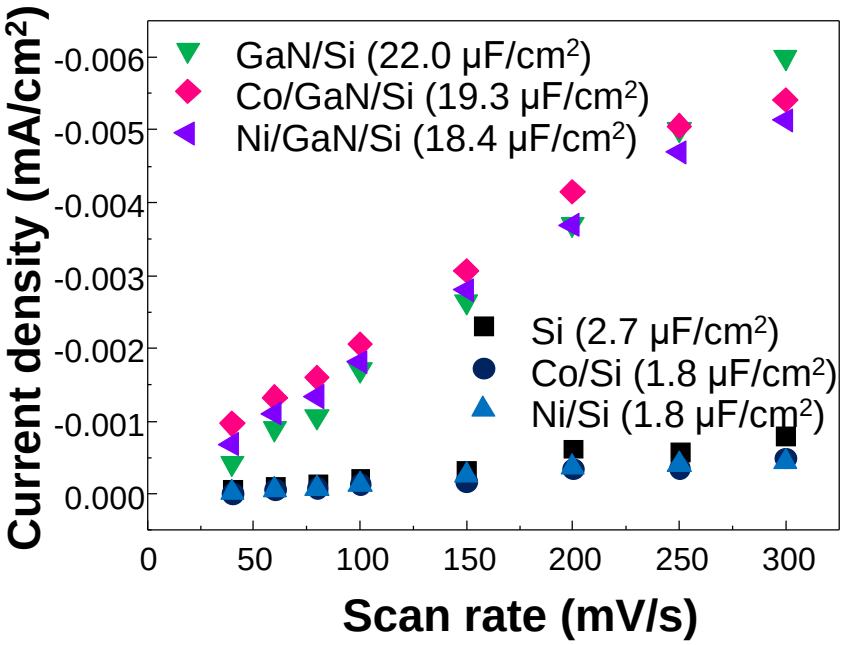

Figure S27. Electrochemical surface area. Current density plots at various scan rates. Double layer capacitance, which linearly correlates to electrochemical surface area (ECSA), can be obtained from the slopes of current density-scan rate curves. ECSA of GaN was ~8 times larger than Si wafer.

Electrochemical active surface area (ECSA) of the photoelectrodes was determined using electrochemical double-layer capacitance as an indirect measure. This method relies on the observation that the capacitive current in the non-faradaic potential region is directly proportional to the scan rate of the cyclic voltammetry (CV). To perform this measurement, CV was conducted in a potential range where no faradaic reactions occur. The capacitive current at a fixed potential was extracted for each scan rate. The capacitive current values were then plotted against the corresponding scan rates (Figure S27), yielding a linear relationship where the slope corresponds to the double-layer capacitance. The presence of the catalyst has a negligible impact on the ECSA, as samples with GaN NWs also exhibited double-layer capacitance values more than 8 times higher. This highlights the dominant role of GaN NWs in increasing the surface area.

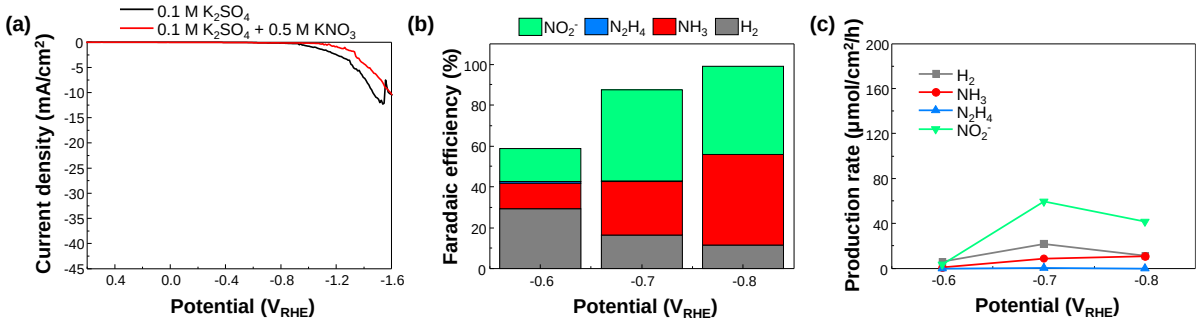

Figure S28. Photoelectrochemical performance of Si. (a) LSV curves of n^+-p Si measured in 0.1 M K_2SO_4 (black) and 0.1 M K_2SO_4 with 0.5 M KNO_3 (red) under AM 1.5G 1-sun light illumination. (b) Faradaic efficiency and (c) production rate of H_2, NH_3, N_2H_4, and NO_2^- at various potentials.

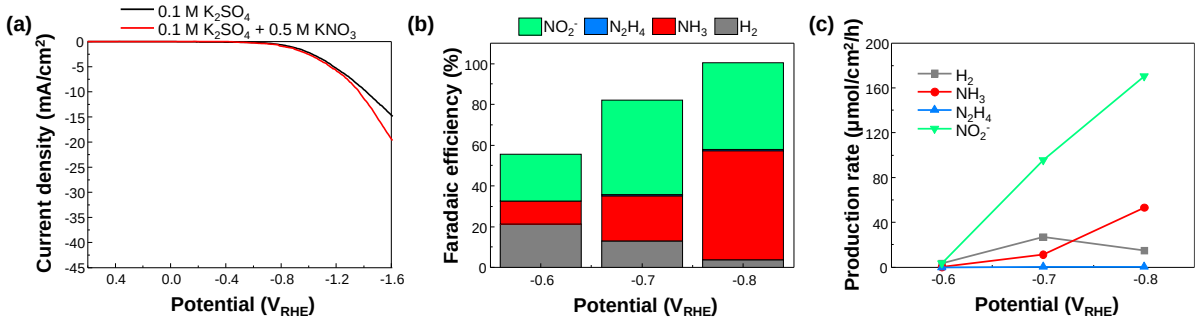

Figure S29. Photoelectrochemical performance of Co/Si. (a) LSV curves of Co/Si measured in 0.1 M K_2SO_4 (black) and 0.1 M K_2SO_4 with 0.5 M KNO_3 (red) under AM 1.5G 1-sun light illumination. (b) Faradaic efficiency and (c) production rate of H_2, NH_3, N_2H_4, and NO_2^- at various potentials.

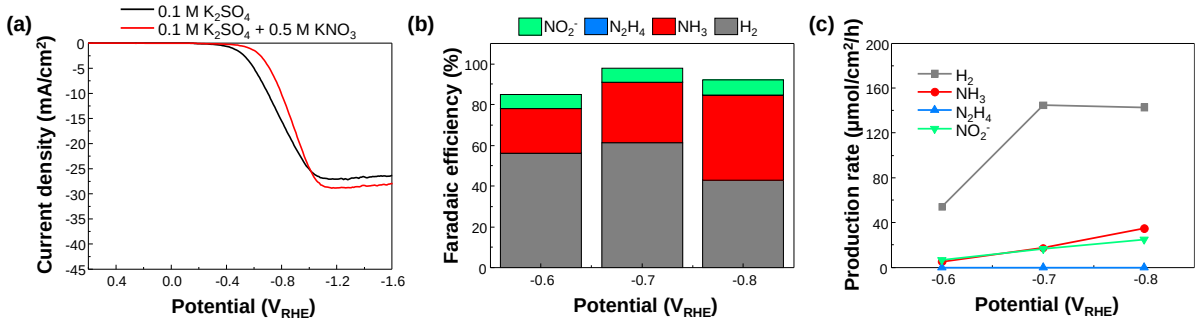

Figure S30. Photoelectrochemical performance of Ni/Si. (a) LSV curves of Ni/Si measured in 0.1 M K_2SO_4 (black) and 0.1 M K_2SO_4 with 0.5 M KNO_3 (red) under AM 1.5G 1-sun light illumination. (b) Faradaic efficiency and (c) production rate of H_2, NH_3, N_2H_4, and NO_2^- at various potentials.

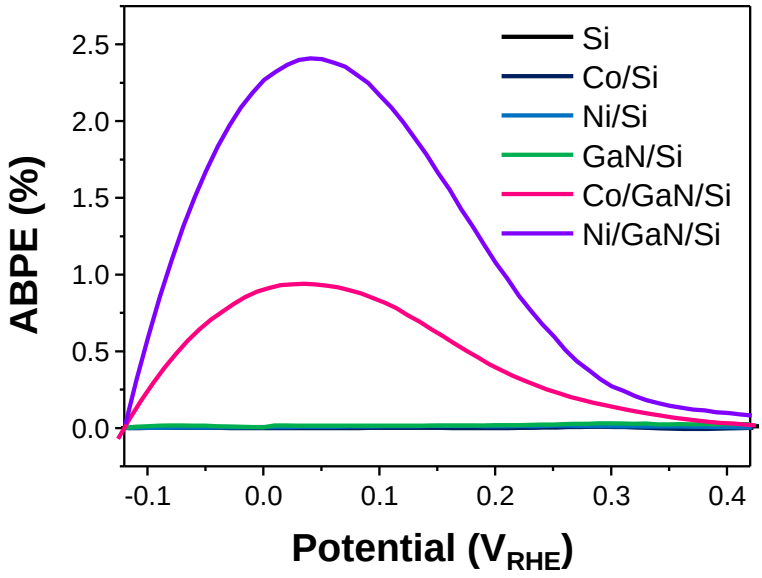

Figure S31. Applied bias photon-to-current efficiency. Applied bias photon-to-current efficiency (ABPE) for the tested photoelectrodes.

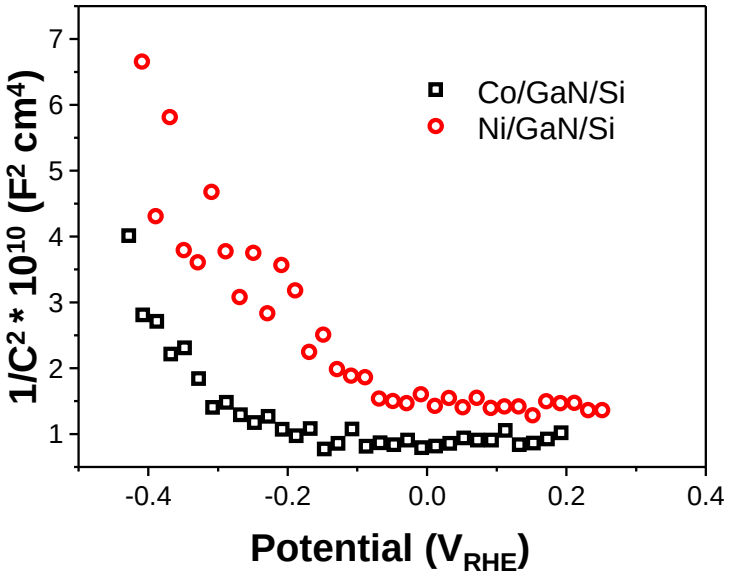

Figure S32. Mott–Schottky analysis. Mott–Schottky plots of Co/GaN/Si and Ni/GaN/Si photoelectrodes. The measurements were conducted at a frequency of 0.3 kHz and an amplitude of 20 mV.

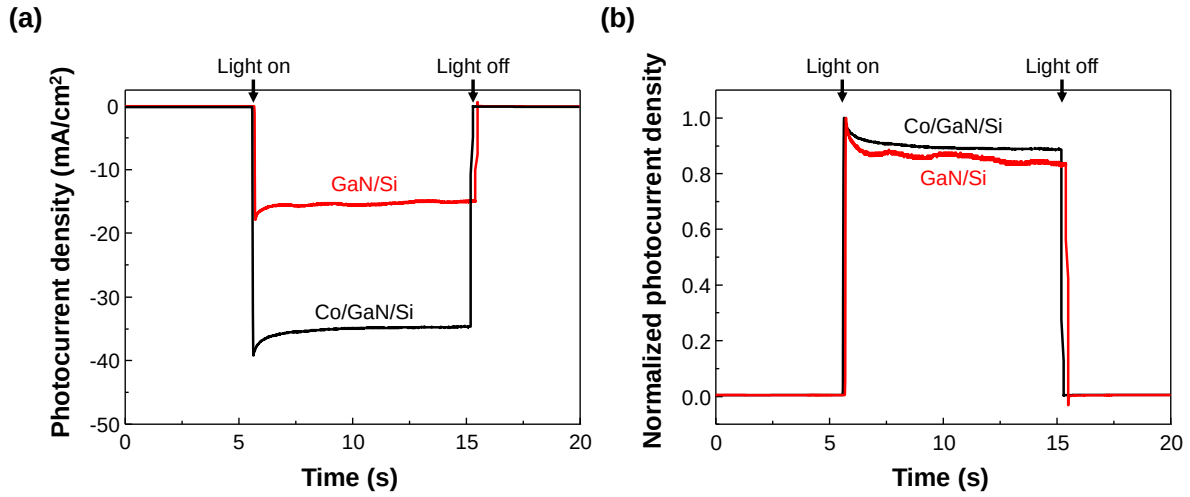

Figure S33. Transient photocurrent measurement. (a) Transient photocurrent density measurements of GaN/Si and Co/GaN/Si photoelectrodes at -0.4 V_{RHE} under chopped illumination. (b) Normalized transient photocurrent density curves.

Transient photocurrent density measurements at -0.4 V_{RHE} (Figure S33a) reveal critical differences in charge transfer dynamics and recombination behavior between Co/GaN/Si and GaN/Si. Upon illumination, both systems exhibit a sharp photocurrent rise, but Co/GaN/Si achieves a significantly higher steady-state photocurrent, indicating enhanced charge transfer facilitated by the Co catalyst. Co/GaN/Si also shows a more gradual decay, reflecting better charge retention.[17] This trend is further emphasized in the normalized curves (Figure S33b), where Co/GaN/Si demonstrates a smoother transition and reduced recombination compared to the sharper spikes and faster decay of GaN/Si. These findings highlight the catalytic role of Co in improving charge transfer efficiency and suppressing recombination in Co/GaN/Si.

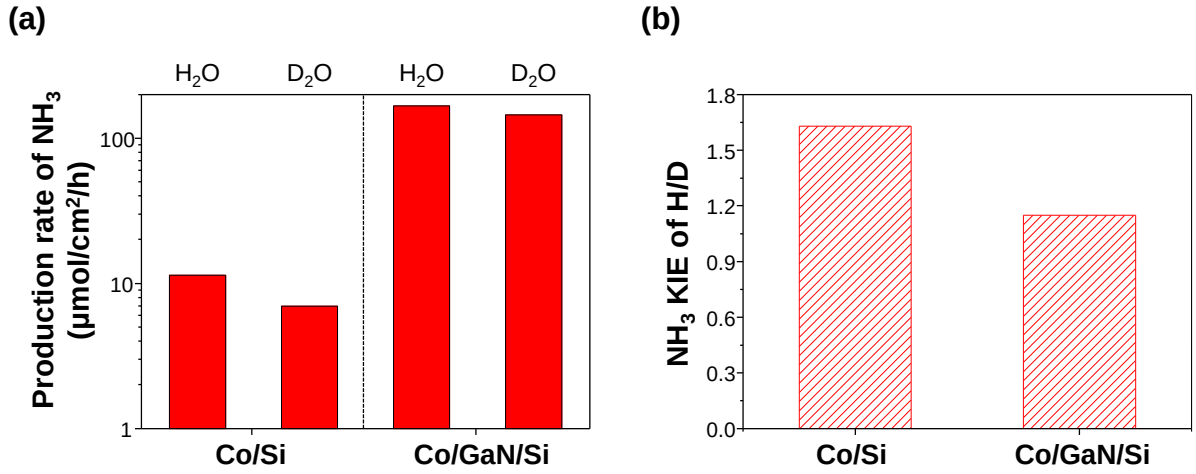

Figure S34. Kinetic isotope effect. (a) Production rate of NH_3 in 0.1 M K_2SO_4 and 0.5 M KNO_3 with H_2O and D_2O solvents. The measurements were conducted at -0.7 V_{RHE}. (b) Calculated KIE value of H/D for Co/Si and Co/GaN/Si photoelectrodes.

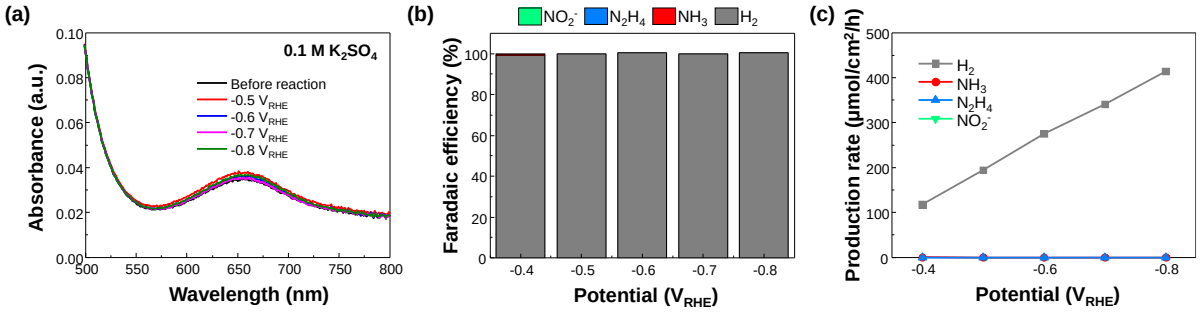

Figure S35. Control experiment without nitrate. (a) UV-visible spectra of indophenol assays that were prepared using Co/GaN/Si in 0.1 M K_2SO_4 at various potentials. (b) Faradaic efficiency and (c) production rate of H_2, NH_3, N_2H_4, and NO_2^- at various potentials. FE_{H2} approaches to ~100%, indicating that NH_3, N_2H_4, and NO_2^- were not produced without presence of NO_3^- in the solution.

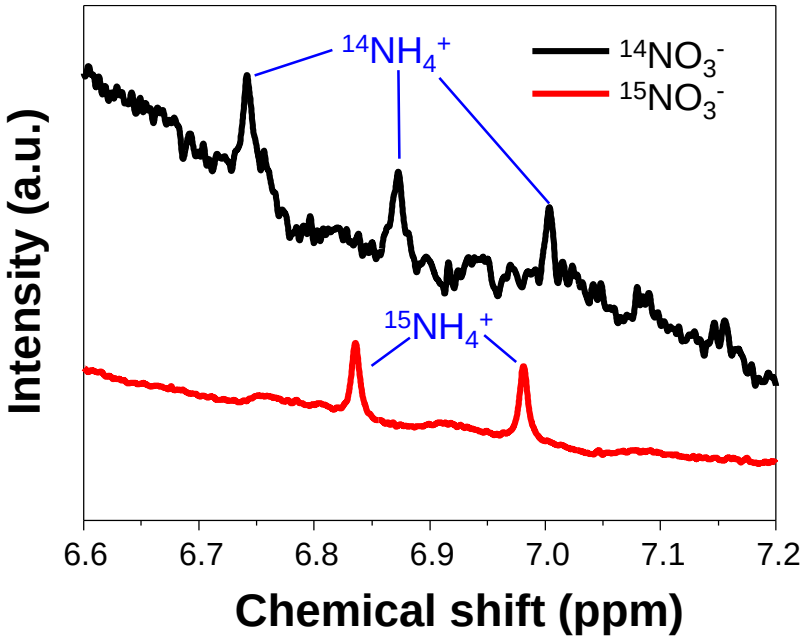

Figure S36. Isotope labeling test. ^{1}H NMR spectra of the electrolytes after NO_3^-RR using $K^{14}NO_3$ and $K^{15}NO_3$ as the nitrogen source. Co/GaN/Si was used in 0.1 M K_2SO_4 with 0.5 M KNO_3 at -0.6 V_{RHE}. Typical triple and double peaks of NH_4^+ were observed with reactants of $^{14}NO_3^-$ and $^{15}NO_3^-$, respectively.

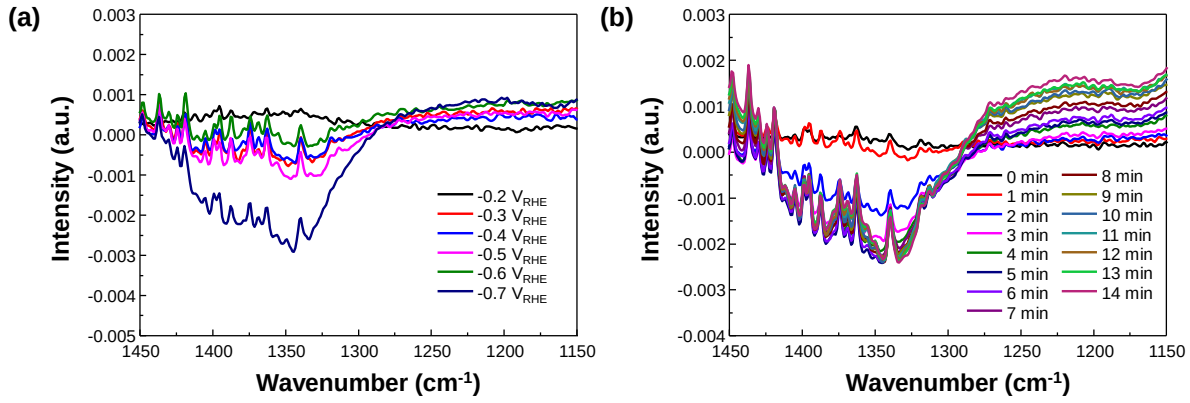

Figure S37. In-situ FTIR measurement of GaN/Si. *In-situ* FTIR spectra of GaN/Si photoelectrode during PEC NO_3^-RR. (a) Potential-dependent spectra from -0.2 to -0.7 V_{RHE} and (b) time-resolved spectra at -0.5 V_{RHE}.

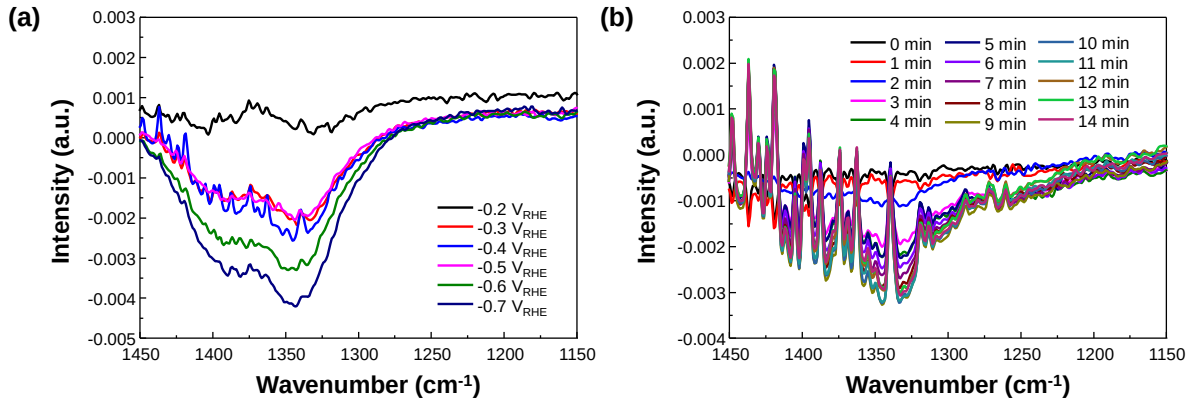

Figure S38. In-situ FTIR measurement of Co/GaN/Si. *In-situ* FTIR spectra of Co/GaN/Si photoelectrode during PEC NO_3^-RR. (a) Potential-dependent spectra from -0.2 to -0.7 V_{RHE} and (b) time-resolved spectra at -0.5 V_{RHE}.

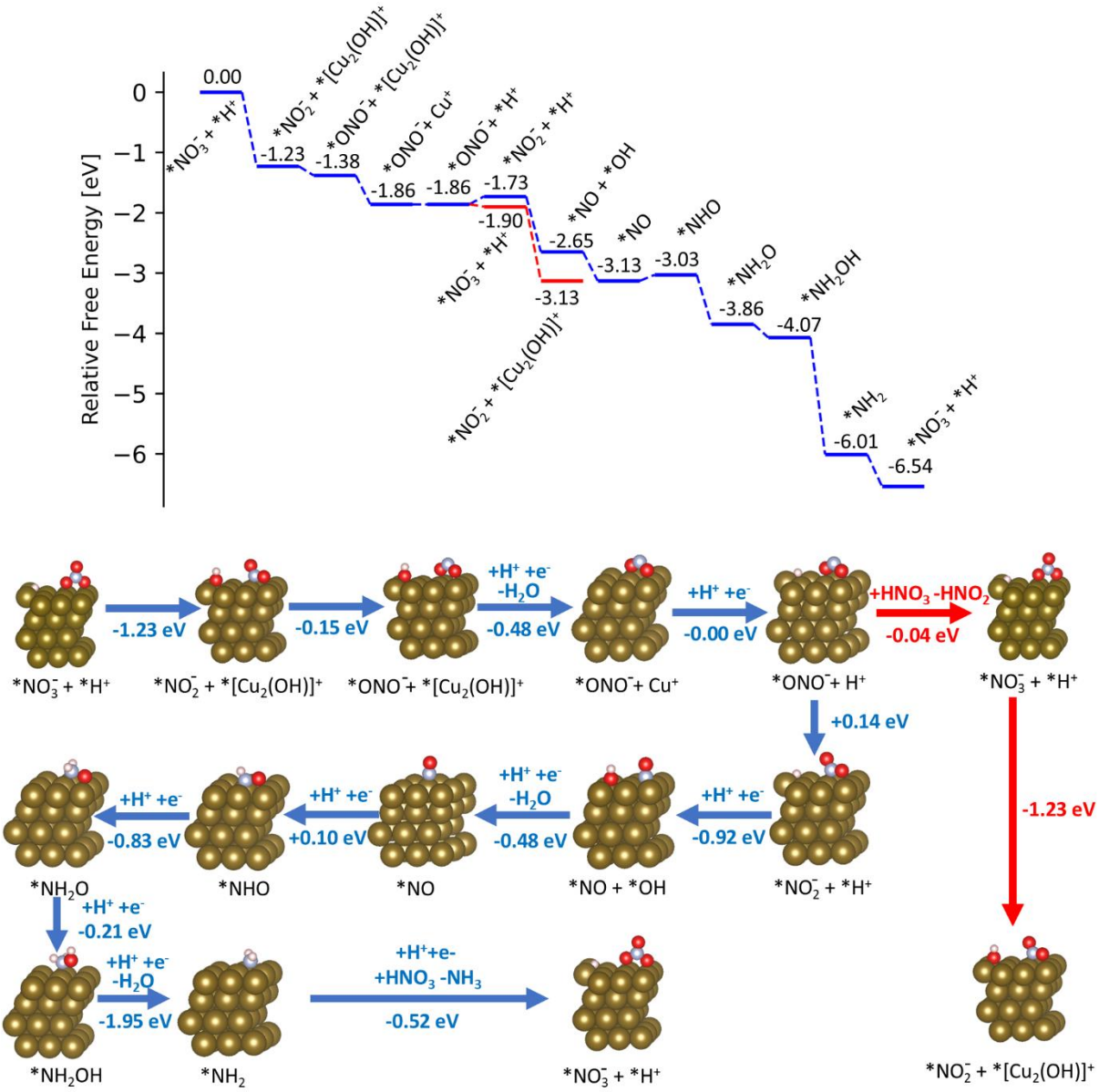

Figure S39. Photoelectrochemical nitrate reduction on Cu. Relative Gibbs free energies for the two possible reaction pathways in photoelectrochemical NO_3^- reduction on Cu. Given in blue are the full reduction to ammonia, while the incomplete reduction to NO_2^- and subsequent desorbtion is given in red. On Cu, incomplete reduction to NO_2^- is preferred due to it's low binding energy on Cu, leading to NO_2^- as the main product. The optimized structures and Gibbs free energy differences for each step are given as well.

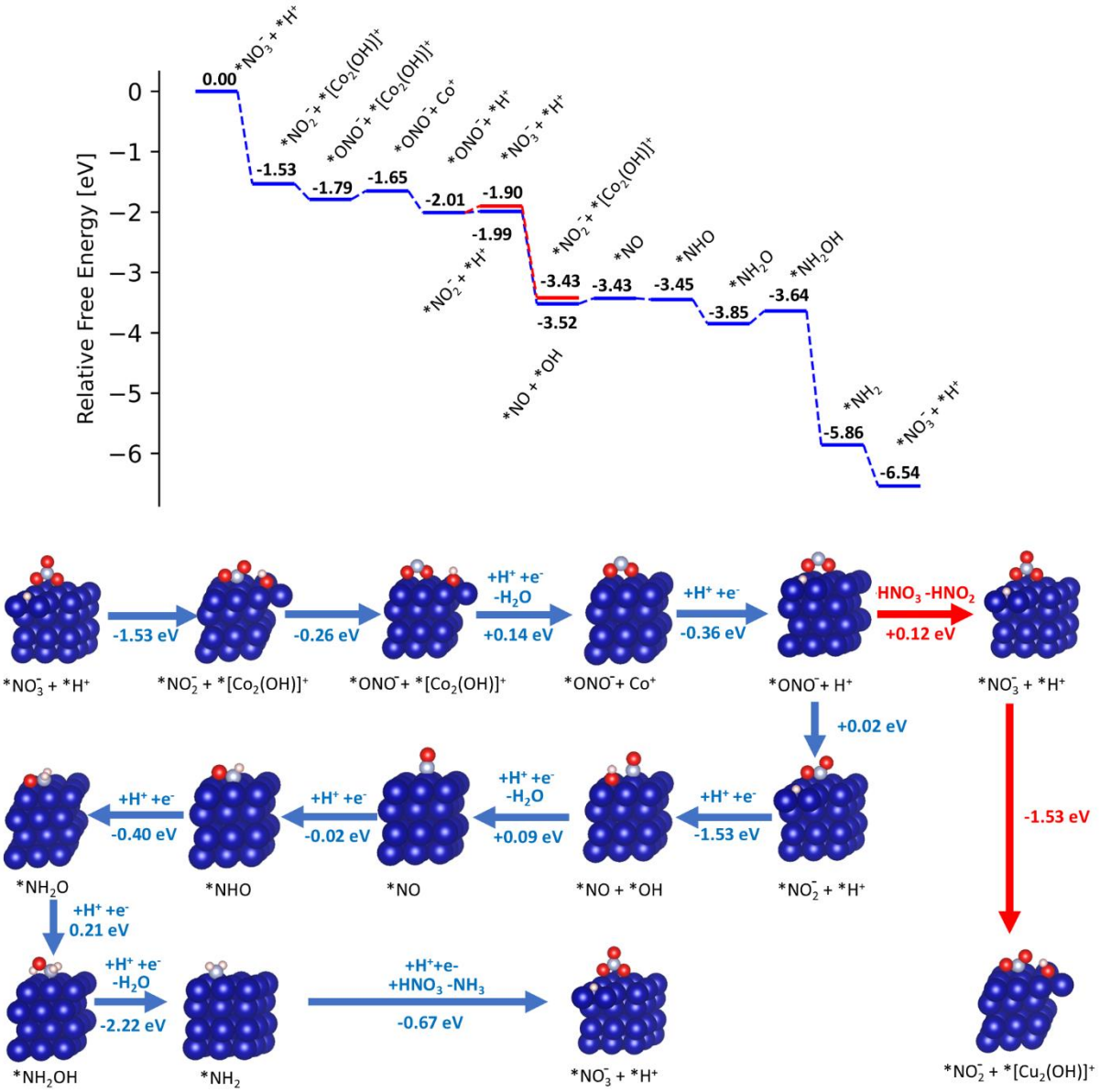

Figure S40. Photoelectrochemical nitrate reduction on Co. Relative Gibbs free energies for the two possible reaction pathways in photoelectrochemical NO_3^- reduction on Co. Given in blue are the full reduction to ammonia, while the incomplete reduction to NO_2^- and subsequent desorbtion is given in red. On Co, full reduction to ammonia is the preferred pathway leading to ammonia as main product. The optimized structures and Gibbs free energy differences for each step are given as well.

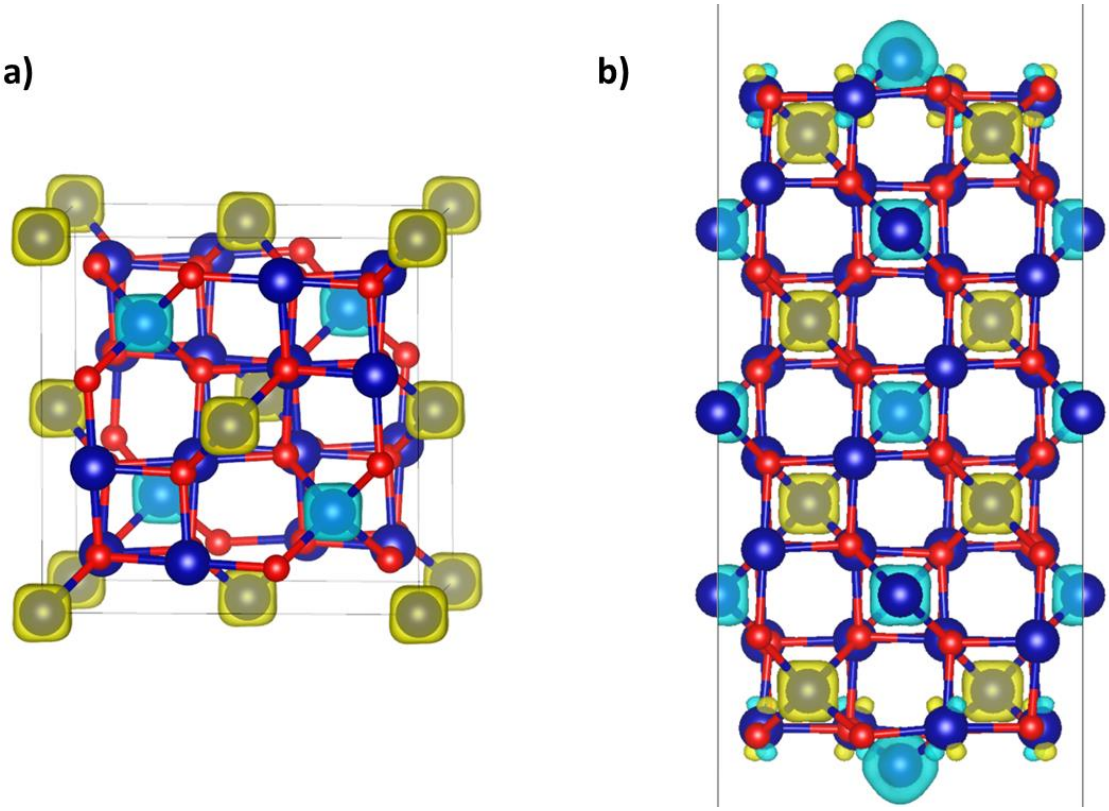

Figure S41. DFT+U model of Co_3O_4. Geometry and spin structure of (a) bulk Co_3O_4 and the (b) 100-S surface with α spin density given in yellow and β spin density in cyan.

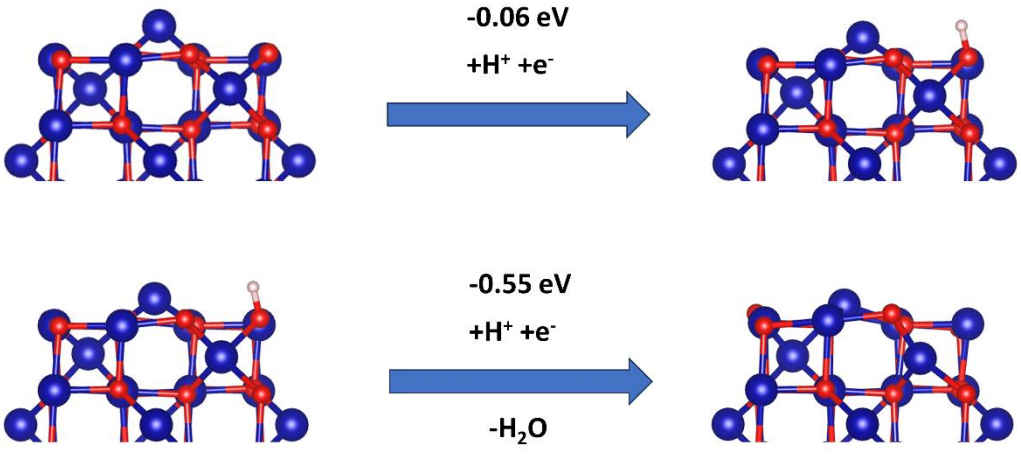

Figure S42. Reductive defect formation on Co_3O_4. First reduction leads to an O*H species that can be further reduced to release water, leaving an oxygen defect.

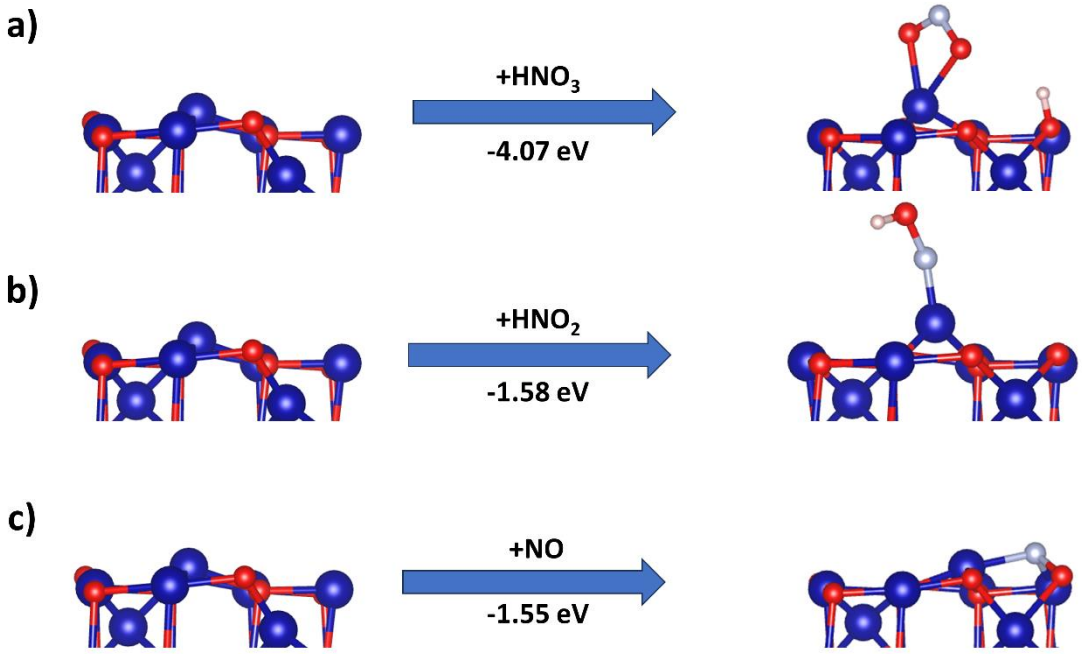

Figure S43. Oxygen defect reactivity. Reactivity of an O-defect on Co_3O_4 towards (a) HNO_3, (b) HNO_2 and (c) NO respectively.

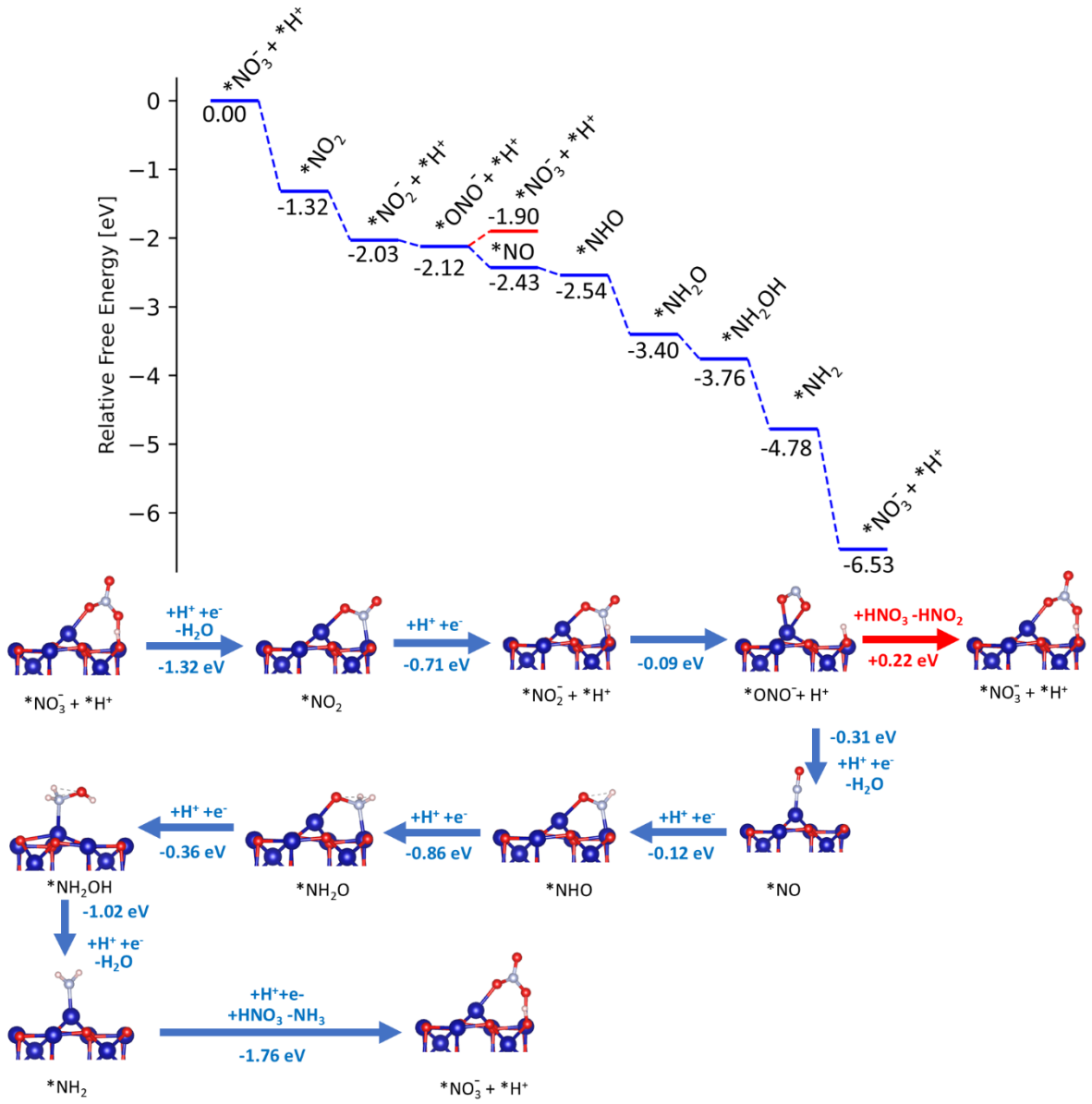

Figure S44. Photoelectrochemical nitrate reduction on Co_3O_4. Relative Gibbs free energies for the photoelectrochemical NO_3^- reduction on Co_3O_4. Given in blue are the full reduction to ammonia, while the incomplete reduction to NO_2^- and subsequent desorption is given in red.

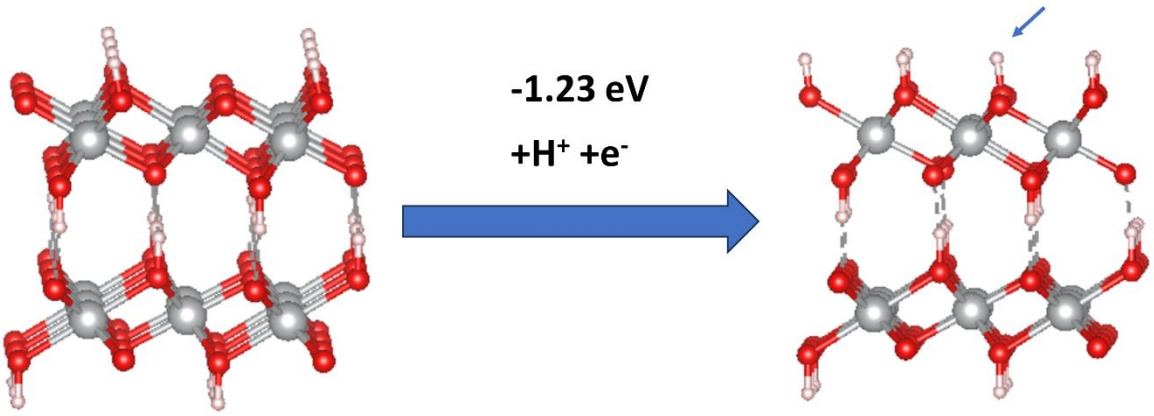

Figure S45. Reduction of NiOOH under irradiation. Reduction of NiOOH to $Ni(OH)_2$ using photogenerated electrons is highly favorable under irraditation condition.

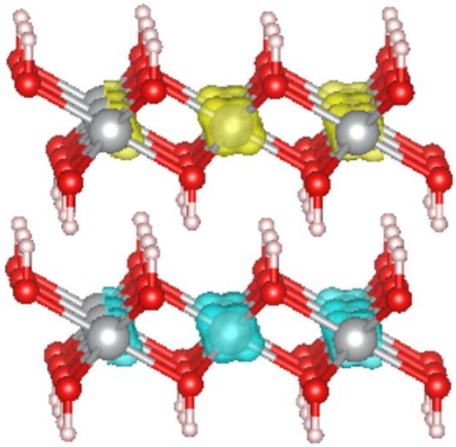

Figure S46. DFT+U model of $Ni(OH)_2$. Geometry and spin structure of 001 surface of $Ni(OH)_2$ with α spin density given in yellow and β spin density in cyan.

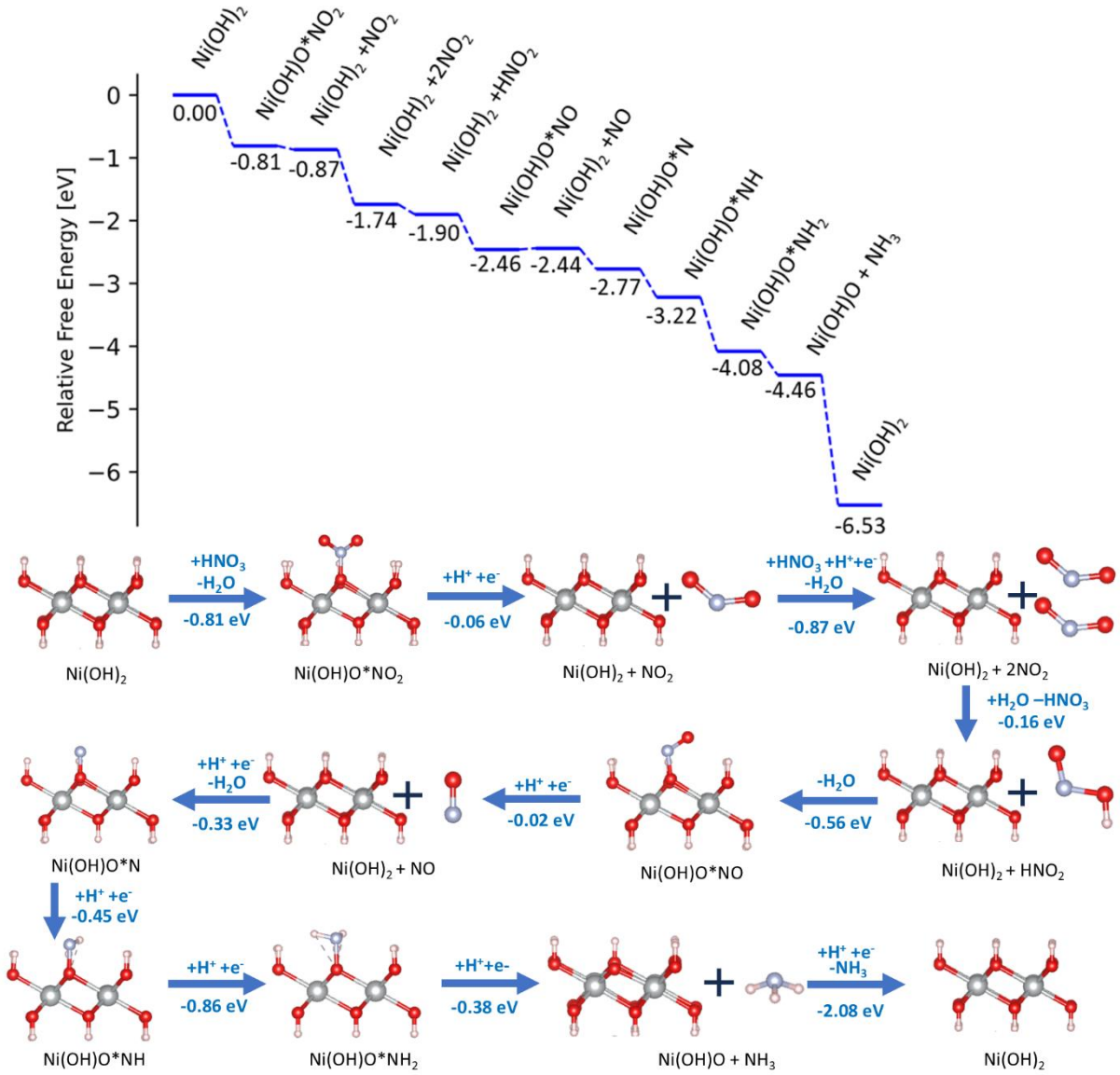

Figure S47. Photoelectrochemical nitrate reduction on $Ni(OH)_2$. Relative Gibbs free energies for the photoelectrochemical NO_3^- reduction on $Ni(OH)_2$. Nitric acid reacts in an acid base reaction with $Ni(OH)_2$ to release a water and then filling the generated defect. Further reduction releases NO_2. The NO_2 reacts with another NO_2 molecule and water to regenerate one HNO_3 molecule and form nitrous acid (HNO_2), which can react with $Ni(OH)_2$ in a similar matter, resulting in the Ni(OH)O*NO species. Reduction releases NO, that can react again under protonation and reduction with $Ni(OH)_2$. Further reduction to Ni(OH)O*NH and $Ni(OH)O*NH_2$ is thermodynamically favorable, as is the release of NH_3. Regerneration of the Ni(OH)O to $Ni(OH)_2$ completes the catalytic cycle.

Table S1. Performance comparison of electrochemical (EC) and photoelectrochemical (PEC) NO_3^- reduction from recent literature.

EC/PEC	Cathode	Electrolyte	Potential	FE_{NH3}	Y_{NH3}	Ref.
EC	Cu-PTCDA	0.1 M PBS with 500 ppm $NaNO_3$	-0.4 V_{RHE}	85.9%	25.6 μmol/cm²/h	18
EC	CuNi alloy	0.1 M KOH with 0.1 M KNO_3	-0.15 V_{RHE}	99%	J_{NH3} = -90 mA/cm²	19
EC	Strained Ru nanocluster	1 M KOH with 1 M KNO_3	-0.2 V_{RHE}	~100%	1.17 mmol/cm²/h	20
EC	Cu/Cu_2O nanowire	0.5 M Na_2SO_4 with 200 ppm of $NaNO_3$	-0.85 V_{RHE}	95.8%	244.9 μmol/cm²/h	21
EC	Fe SAC	0.1 M K_2SO_4 with 0.5 M KNO_3	-0.66 V_{RHE}	~75%	~121 μmol/cm²/h	22
EC	Fe-MoS_2	0.1 M $NaSO_4$, 0.1 M NaOH with 0.1 $NaNO_3$	-0.48 V_{RHE}	98%	J_{NH3} = -8.4 mA/cm²	23
EC	Fe-PPy SACs	0.1 M KOH with 0.1 M KNO_3	-0.7 V_{RHE}	~100%	2.75 mg_{NH3}/cm²/h	24
EC	Oxide-derived Co	1 M KOH with 1 M KNO_3	-0.8 V_{RHE}	92.37%	J_{NH3} = -565.26 mA/cm²	25
EC	CuCoSP	0.1 M KOH with 0.1 M KNO_3	-0.175 V_{RHE}	93.3%	1.17 mmol/cm²/h	26
EC	Rh@Cu nanowire	0.1 M Na_2SO_4 with 0.1 M KNO_3	-0.2 V_{RHE}	93%	J_{NH3} = -162 mA/cm²	27
EC	Bi-Cl_{red}	1 M KOH with 0.5 M KNO_3	-0.5 V_{RHE}	90.6%	~11 $g_{NH3}/h/g_{cat}$	28
EC	RhCu nanocube	0.01 M $HClO_4$ with 0.05 M KNO_3	0.05 V_{RHE}	93.7%	2.4 $g_{NH3}/h/g_{cat}$	29
EC	CoP nanosheet	1 M NaOH with 1 M $NaNO_3$	-0.3 V_{RHE}	~100%	956 μmol/cm²/h	30
EC	Pd-NDs/Zr-MOF	0.1 M Na_2SO_4 with 500 ppm $NaNO_3$	-1.3 V_{RHE}	58.1%	287.31 mmol/h/g_{cat}	31
EC	$NiCo_2O_4$ nanowire	0.1 M NaOH with 0.1 M $NaNO_3$	-0.6 V_{RHE}	99%	973.2 μmol/cm²/h	32
EC	Cu@C	1 M KOH with 0.001 M KNO_3	-0.3 V_{RHE}	72.0%	27.6 μmol/cm²/h at -0.9 V_{RHE}	33
EC	Cu-*cis*-N_2O_2	0.5 M Na_2SO_4 with 0.1 M KNO_3	-2.0 V_{RHE}	>70%	1690 μmol/cm²/h	34
PEC	O-SiNW/Au	0.5 M K_2SO_4 with 10 mM KNO_3	0.2 V_{RHE}	95.6%	0.26 μmol/cm²/h	35
PEC	CoCu/TiO_2/Sb_2Se_3	10 mM H_2SO_4 with 0.1 M KNO_3	-0.2 V_{RHE}	88.01%	15.91 μmol/cm²/h at -0.3 V_{RHE}	36
PEC	CuSn/TiO_2/Sb_2S_3	10 mM H_2SO_4 with 0.1 M KNO_3	0.4 V_{RHE}	97.82%	15.91 μmol/cm²/h at 0 V_{RHE}	37
PEC	Co/GaN/Si	0.1 M K_2SO_4 with 0.5 KNO_3	0.2 V_{RHE}	~100%	4.9 μmol/cm²/h	This work
	Ni/GaN/Si	0.1 M K_2SO_4 with 0.5 KNO_3	-0.4 V_{RHE}	99%	195.3 μmol/cm²/h	

Table S2. Electronic energies in implicit solvent, Gibbs free energy corrections and Gibbs free energy of all intermediates on Cu.

Intermediate	Electronic energy [eV]	Free energy correction term [eV]	Gibbs free energy [eV]
Cu slab	-142.361	+0.000	-142.361
$*NO_3^- *H^+$	-171.836	+0.435	-171.402
$*ONO^- (Cu_2OH)^+$	-173.246	+0.463	-172.783
$*NO_2^- (Cu_2OH)^+$	-173.097	+0.463	-172.634
$*ONO^- Cu^+$	-162.362	+0.159	-162.203
$*NO_2^- Cu^+$	-162.206	+0.177	-162.029
$*ONO^- *H^+$	-165.930	+0.331	-165.599
$*NO_2^- *H^+$	-165.811	+0.348	-165.463
$*NO (Cu_2OH)^+$	-166.795	+0.410	-166.385
*NO	-155.823	+0.016	-155.807
*NHO	-159.509	+0.407	-159.102
*NHOH	-163.673	+0.717	-162.956
NH	-154.098	+0.354	-153.743
$*NH_2O$	-164.088	+0.765	-163.322
$*NH_2OH$	-167.896	+0.967	-166.929
$*NH_2$	-158.457	+0.642	-157.815

Table S3. Electronic energies in implicit solvent per spin state giving the number of unpaired electrons (the lowest marked in bold), Gibbs free energy corrections and Gibbs free energy of all intermediates on Co.

Intermediate	Electronic energy [eV]					Free energy correction term [eV]	Gibbs free energy [eV]
	55	56	57	58	59		
Co slab		-251.698	**-251.876**	-251.803		+0.000	-251.876
$*NO_3^- *H^+$		-282.011	**-282.115**	-282.110		+0.461	-281.654
$*ONO^- (Co_2OH)^+$			-283.908	**-283.947**	-283.932	+0.505	-283.442
$*NO_2^- (Co_2OH)^+$			-283.869	**-283.894**	-283.872	+0.507	-283.387
$*ONO^- Co^+$			-272.408	**-272.422**	-272.317	+0.178	-272.245
$*NO_2^- Co^+$		-272.316	**-272.389**	-272.381		+0.176	-272.214
$*ONO^- *H^+$		-276.307	**-276.368**	-276.350		+0.367	-276.001
$*NO_2^- *H^+$		-276.296	**-276.330**	-276.298		+0.352	-275.978
$*NO (Co_2OH)^+$		-277.908	**-277.936**	-277.858		+0.427	-277.509
*NO	-266.410	**-266.481**	-266.410			+0.121	-266.360
*NHO		-270.182	**-270.195**	-270.191		+0.416	-269.775
*NHOH			-274.028	**-274.047**	-273.951	+0.710	-273.337
NH		-264.890	**-264.903**	-264.868		+0.366	-264.537
$*NH_2O$			-274.291	**-274.336**	-274.237	+0.774	-273.563
$*NH_2OH$		-277.668	**-277.765**	-277.687		+1.016	-276.749
$*NH_2$			-268.540	**-268.553**	-268.464	+0.639	-267.914

Table S4. Electronic energies in implicit solvent, Gibbs free energy corrections and Gibbs free energy of all intermediates on Co_3O_4. For intermediates with an uneven number of electrons, the magnetization of lower energy is provided.

Intermediate		Electronic energy [eV]	Free energy correction term [eV]	Gibbs free energy [eV]
Co_3O_4		-693.579	+0.000	-693.579
*H (spin=1)	Without O	-697.343	+0.312	-697.031
	Including O frequencies	-697.343	+0.375	-696.968
O defect (Co_3O_3)		-686.455	+0.000	-686.455
$*NO_3^-$ $*H^+$		-725.706	+0.585	-725.120
$*ONO^-$ Cu^+ (spin=1)		-715.358	+0.226	-715.131
$*NO_2^-$ Cu^+ (spin=0)		-715.614	+0.236	-715.377
$*ONO^-$ $*H^+$	Without O	-720.055	+0.481	-719.574
	Including O frequencies	-720.055	+0.544	-719.511
$*NO_2^-$ $*H^+$	Without O	-720.018	+0.537	-719.481
	Including O frequencies	-720.018	+0.614	-719.404
*NO (spin=1)	Without O	-708.901	+0.081	-708.819
	Including O frequencies	-708.901	+0.146	-708.755
*NHO		-712.773	+0.441	-712.332
*NOH	Without O	-711.686	+0.356	-711.330
	Including O frequencies	-711.686	+0.423	-711.263
*NHOH (spin=1)		-717.056	+0.720	-716.336
*NH		-705.554	+0.238	-705.316
$*NH_2O$ (spin=0)		-717.400	+0.811	-716.590
$*NH_2OH$		-721.388	+1.047	-720.341
$*NH_2$ (spin=0)		-710.861	+0.564	-710.297
*N (spin=1)	Without O	-700.870	+0.103	-700.767
	Including O frequencies	-700.870	+0.160	-700.710

Table S5. Electronic energies in implicit solvent, Gibbs free energy corrections and Gibbs free energy of all intermediates on $Ni(OH)_2$.

Intermediate	Electronic energy [eV]	Free energy correction term [eV]	Gibbs free energy [eV]
$Ni(OH)_2$	-203.631	+0.355	-203.276
Ni(OH)(O)	-197.861	+0.056	-197.805
Ni(OH)X	-191.251	+0.000	-191.251
$Ni(OH)O*NO_2$	-218.924	+0.300	-218.624
Ni(OH)O*NO	-212.759	+0.153	-212.606
Ni(OH)O*N	-205.341	+0.088	-205.253
Ni(OH)O*NH	-209.468	+0.375	-209.093
$Ni(OH)O*NH_2$	-214.096	+0.743	-213.353
Ni(OH)O*NHO	-215.946	+0.490	-215.457
Ni(OH)O*NOH	+215.839	+0.448	-215.391

Table S6. Electronic energies in implicit solvent, Gibbs free energy corrections and Gibbs free energy of all molecular intermediates. Electronic energies of H_2, NO and NO_2 are in vacuum.

Intermediate	Electronic energy [eV]	Free energy correction term [eV]	Gibbs free energy [eV]
HNO_3	-28.995	-0.010	-28.992
HNO_2	-23.099	-0.125	-23.224
NH_3	-19.744	+0.422	-19.322
H_2O	-14.545	+0.087	-14.458
H_2	-6.769	-0.023	-6.792
NO (spin1)	-12.280	-0.425	-12.706
NO_2 (spin1)	-18.396	-0.404	-18.800

Supplementary References

1. Kresse G, Hafner J. Ab initio molecular dynamics for liquid metals. *Phys. Rev. B* **47**, 558 (1993).

2. Kresse G, Furthmüller J. Efficiency of ab-initio total energy calculations for metals and semiconductors using a plane-wave basis set. *Comput. Mater. Sci.* **6**, 15-50 (1996).

3. Kresse G, Furthmüller J. Efficient iterative schemes for ab initio total-energy calculations using a plane-wave basis set. *Phys. Rev. B* **54**, 11169 (1996).

4. Kresse G, Hafner J. Norm-conserving and ultrasoft pseudopotentials for first-row and transition elements. *J. Phys. Condens. Matter* **6**, 8245 (1994).

5. Kresse G, Joubert D. From ultrasoft pseudopotentials to the projector augmented-wave method. *Phys. Rev. B* **59**, 1758 (1999).

6. Perdew JP, Burke K, Ernzerhof M. Generalized gradient approximation made simple. *Phys. Rev. Lett.* **77**, 3865 (1996).

7. Grimme S, Antony J, Ehrlich S, Krieg H. A consistent and accurate ab initio parametrization of density functional dispersion correction (DFT-D) for the 94 elements H-Pu. *J. Chem. Phys.* **132**, 154104 (2010).

8. Grimme S, Ehrlich S, Goerigk L. Effect of the damping function in dispersion corrected density functional theory. *J. Comput. Chem.* **32**, 1456-1465 (2011).

9. Methfessel M, Paxton A. High-precision sampling for Brillouin-zone integration in metals. *Phys. Rev. B* **40**, 3616 (1989).

10. Selcuk S, Selloni A. DFT+ U study of the surface structure and stability of Co_3O_4 (110): dependence on U. *J. Phys. Chem. C* **119**, 9973-9979 (2015).

11. Monkhorst HJ, Pack JD. Special points for Brillouin-zone integrations. *Phys. Rev. B* **13**, 5188 (1976).

12. Zhao Q, Kulik HJ. Where does the density localize in the solid state? Divergent behavior for hybrids and DFT+ U. *J. Chem. Theory Comput.* **14**, 670-683 (2018).

13. Kim B*, et al.* Vertical-crystalline Fe-doped β-Ni oxyhydroxides for highly active and stable oxygen evolution reaction. *Matter* **4**, 3585-3604 (2021).

14. Wang V, Xu N, Liu J-C, Tang G, Geng W-T. VASPKIT: A user-friendly interface facilitating high-throughput computing and analysis using VASP code. *Comput. Phys. Commun.* **267**, 108033 (2021).

15. Mathew K, Sundararaman R, Letchworth-Weaver K, Arias T, Hennig RG. Implicit solvation model for density-functional study of nanocrystal surfaces and reaction pathways. *J. Chem. Phys.* **140**, 084106 (2014).

16. Momma K, Izumi F. VESTA 3 for three-dimensional visualization of crystal, volumetric and morphology data. *J. Appl. Crystallogr.* **44**, 1272-1276 (2011).

17. Peter LM, Walker AB, Bein T, Hufnagel AG, Kondofersky I. Interpretation of photocurrent transients at semiconductor electrodes: Effects of band-edge unpinning. *J. Electroanal. Chem.* **872**, 114234 (2020).

18. Chen G-F, *et al.* Electrochemical reduction of nitrate to ammonia via direct eight-electron transfer using a copper–molecular solid catalyst. *Nat. Energy* **5**, 605-613 (2020).

19. Wang Y, *et al.* Enhanced nitrate-to-ammonia activity on copper–nickel alloys via tuning of intermediate adsorption. *J. Am. Chem. Soc.* **142**, 5702-5708 (2020).

20. Li J, *et al.* Efficient ammonia electrosynthesis from nitrate on strained ruthenium nanoclusters. *J. Am. Chem. Soc.* **142**, 7036-7046 (2020).

21. Wang Y, Zhou W, Jia R, Yu Y, Zhang B. Unveiling the activity origin of a copper-based electrocatalyst for selective nitrate reduction to ammonia. *Angew. Chem. Int. Ed.* **59**, 5350-5354 (2020).

22. Wu Z-Y, *et al.* Electrochemical ammonia synthesis via nitrate reduction on Fe single atom catalyst. *Nat. Commun.* **12**, 1-10 (2021).

23. Li J, *et al.* 3.4% Solar-to-Ammonia Efficiency from Nitrate Using Fe Single Atomic Catalyst Supported on MoS_2 Nanosheets. *Adv. Funct. Mater.* **32**, 2108316 (2022).

24. Li P, Jin Z, Fang Z, Yu G. A single-site iron catalyst with preoccupied active centers that achieves selective ammonia electrosynthesis from nitrate. *Energy Environ. Sci.* **14**, 3522-3531 (2021).

25. Kani NC, *et al.* Solar-driven electrochemical synthesis of ammonia using nitrate with 11% solar-to-fuel efficiency at ambient conditions. *Energy Environ. Sci.* **14**, 6349-6359 (2021).

26. He W, *et al.* Splicing the active phases of copper/cobalt-based catalysts achieves high-rate tandem electroreduction of nitrate to ammonia. *Nat. Commun.* **13**, 1-13 (2022).

27. Liu H, *et al.* Efficient Electrochemical Nitrate Reduction to Ammonia with Copper-Supported Rhodium Cluster and Single-Atom Catalysts. *Angew. Chem. Int. Ed.*, **61,** e202202556 (2022).

28. Zhang N, *et al.* Governing Interlayer Strain in Bismuth Nanocrystals for Efficient Ammonia Electrosynthesis from Nitrate Reduction. *ACS Nano* **16**, 4795-4804 (2022).

29. Ge ZX, *et al.* Interfacial Engineering Enhances the Electroactivity of Frame-Like Concave RhCu Bimetallic Nanocubes for Nitrate Reduction. *Adv. Energy Mater.*, 2103916 (2022).

30. Ye S, *et al.* Elucidating the activity, mechanism and application of selective electrosynthesis of ammonia from nitrate on cobalt phosphide. *Energy Environ. Sci.*, **15**, 760-770 (2022).

31. Jiang M, *et al.* Interfacial Reduction Nucleation of Noble Metal Nanodots on Redox-Active Metal–Organic Frameworks for High-Efficiency Electrocatalytic Conversion of Nitrate to Ammonia. *Nano Lett.* **22**, 2529-2537 (2022).

32. Liu Q, *et al.* Ambient ammonia synthesis via electrochemical reduction of nitrate enabled by $NiCo_2O_4$ nanowire array. *Small* **18**, 2106961 (2022).

33. Song Z, Liu Y, Zhong Y, Guo Q, Zeng J, Geng Z. Efficient Electroreduction of Nitrate into Ammonia at Ultra-low Concentrations via Enrichment Effect. *Adv. Mater.*, **34**,

2204306 (2022).

34. Cheng XF*, et al.* Coordination Symmetry Breaking of Single Atom Catalysts for Robust and Efficient Nitrate Electroreduction to Ammonia. *Adv. Mater.*, **34**, 2205767 (2022).

35. Kim HE, Kim J, Ra EC, Zhang H, Jang YJ, Lee JS. Photoelectrochemical Nitrate Reduction to Ammonia on Ordered Silicon Nanowire Array Photocathodes. *Angew. Chem. Int. Ed.*, **61**, e202204117 (2022).

36. Ren S, Gao RT, Nguyen NT, Wang L. Enhanced Charge Carrier Dynamics on Sb_2Se_3 Photocathodes for Efficient Photoelectrochemical Nitrate Reduction to Ammonia. *Angew. Chem. Int. Ed.* **63**, e202317414 (2024).

37. Ren S*, et al.* Enhanced Charge-Carrier Dynamics and Efficient Photoelectrochemical Nitrate-to-Ammonia Conversion on Antimony Sulfide-Based Photocathodes. *Angew. Chem. Int. Ed.* **63**, e202409693 (2024).